SOFT X-RAYS AND EXTREME ULTRAVIOLET RADIATION

Principles and Applications

DAVID ATTWOOD

UNIVERSITY OF CALIFORNIA, BERKELEY
AND
LAWRENCE BERKELEY
NATIONAL LABORATORY

CAMBRIDGE
UNIVERSITY PRESS

Chapter 1

INTRODUCTION

1.1 THE SOFT X-RAY AND EXTREME ULTRAVIOLET REGIONS OF THE ELECTROMAGNETIC SPECTRUM

One of the last regions of the electromagnetic spectrum to be developed is that between ultraviolet and x-ray radiation, generally shown as a dark region in charts of the spectrum. It is a region where there are a large number of atomic resonances, leading to absorption of radiation in very short distances, typically measured in nanometers (nm) or micrometers (microns, μm), in all materials. This has historically inhibited the pursuit and exploration of the region. On the other hand, these same resonances provide mechanisms for both elemental (C, N, O, etc.) and chemical (Si, SiO_2, $TiSi_2$) identification, creating opportunities for advances in both science and technology. Furthermore, because the wavelengths are relatively short, it becomes possible both to see smaller structures as in microscopy, and to write smaller patterns as in lithography. To exploit these opportunities requires advances in relevant technologies, for instance in materials science and nanofabrication. These in turn lead to new scientific understandings, perhaps through surface science, chemistry, and physics, providing feedback to the enabling technologies. Development of the extreme ultraviolet and soft x-ray spectral regions is presently in a period of rapid growth and interchange among science and technology.

Figure 1.1 shows that portion of the electromagnetic spectrum extending from the infrared to the x-ray region, with wavelengths across the top and photon energies along the bottom. Major spectral regions shown are the infrared (IR), which we associate with molecular resonances and heat; the visible region from red to violet, which we associate with color and vision; the ultraviolet (UV), which we associate with sunburn and ionizing radiation; the regions of extreme ultraviolet (EUV) and soft x-rays (SXR), which are the subject of this book; and finally hard x-rays, which we associate with medical and dental x-rays and with the scientific analysis of crystals, materials, and biological samples through the use of diffractive and other techniques.

The extreme ultraviolet is taken here as extending from photon energies of about 30 eV to about 250 eV, with corresponding wavelengths in vacuum extending from about 5 nm to 40 nm.* The soft x-ray region is taken as extending from about 250 eV (just below the carbon

*It is common to express photon energies in this spectral region in electron volts (eV) or thousands of electron volts (keV), where the photon energy is $\hbar\omega$, $\hbar$ is Planck's constant divided by 2π, and $\omega = 2\pi f$

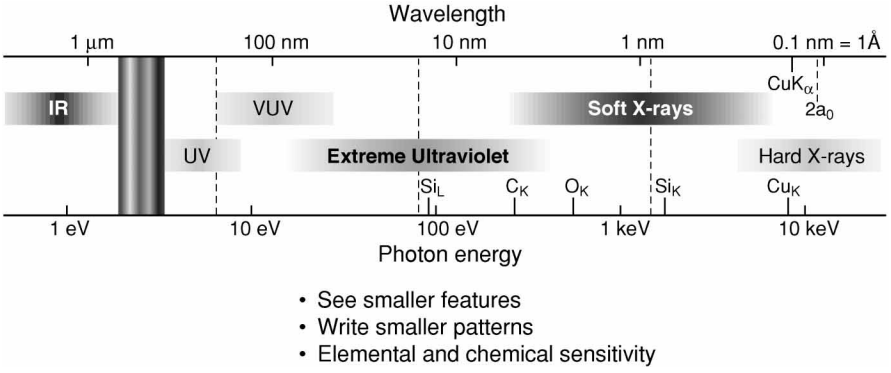

FIGURE 1.1 (see Colorplate I). The electromagnetic spectrum as it extends from the infrared (IR) to the x-ray regions. Visible light is shown with red (650 nm), green (530 nm), and blue (470 nm) wavelengths. At shorter wavelengths are ultraviolet (UV) radiation, extreme ultraviolet radiation (EUV), soft x-rays (SXR), and hard x-rays. Shown for reference are the silicon L-absorption edge at 99.2 eV (12.5 nm wavelength), the carbon K-absorption edge at 284 eV (4.37 nm), the oxygen K-absorption edge at 543 eV (2.28 nm), the silicon K-absorption edge at 1.84 keV (0.674 nm), the copper K-absorption edge at 8.98 keV (0.138 nm), the copper K_α-emission line at 0.154 nm or 1.54 Å (8.05 keV), and twice the Bohr radius at $2a_0 = 1.06$ Å, the diameter of the $n = 1$ orbit in Bohr's model of the hydrogen atom, but more generally a dimension within which resides most of the charge for all atoms. Vertical dashed lines correspond to the transmission limits of common window materials used to isolate vacuum. Shown are approximate transmission limits for common thicknesses of fused silica (pure SiO_2) at 200 nm, a thin film of silicon nitride ($\sim$100 nm thick Si_3N_4) at 15 nm, and an 8 μm thick beryllium foil at a wavelength of about 1 nm.

K-edge) to several keV, as shown in Figure 1.1. These spectral regions are characterized by the presence of the primary atomic resonances and absorption edges of most low and intermediate Z elements, where Z is the atomic number (the number of protons in the nucleus). The primary atomic absorption edges[†] for selected elements are given in Table 1.1, along with $1/e$ absorption lengths at photon energies of 100 eV and 1 keV. The K- and L-absorption edges, associated with the removal of a core electron by photoabsorption from the most tightly bound atomic states (orbitals of principal quantum numbers $n = 1$ and $n = 2$, respectively), are described later in this chapter. The K-absorption edges of carbon (C_K), oxygen, silicon, and copper are shown in Figure 1.1, as is the L-absorption edge of silicon (Si_L), just below 100 eV.

We see in Table 1.1 that many of these absorption edges lie in the combined soft-x-ray and extreme ultraviolet spectral region. What differentiates these regions from neighboring spectral regions is the high degree of absorption in all materials. At lower photon energies, in the visible and ultraviolet, and at higher photon energies, in the hard x-ray region, many materials become transparent and it is not necessary to utilize vacuum isolation techniques in general. For example, Figure 1.1 shows dashed vertical lines at the locations of common window materials that can hold vacuum over square centimeter areas while still transmitting radiation in the indicated regions. In the UV, fused silica, a form of pure SiO_2, is transmissive to wavelengths as short as 200 nm, in millimeter thickness. For shorter wavelengths one quickly enters the vacuum ultraviolet (VUV), where air and all materials are absorbing. Shown just

is the radian frequency. Wavelengths (λ) are commonly expressed in nanometers (1 nm $= 10^{-9}$ m) and angstroms (1 Å $= 10^{-10}$ m). See Appendix A for the values of physical constants and conversion factors.

[†]Standard reference data for this spectral region are given in Refs. 1–4.

Chapter 2

RADIATION AND SCATTERING AT EUV AND SOFT X-RAY WAVELENGTHS

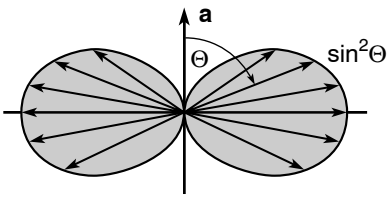

$$\frac{dP}{d\Omega} = \frac{e^2|\mathbf{a}|^2 \sin^2\Theta}{16\pi^2\epsilon_0 c^3} \tag{2.34}$$

$$r_e = \frac{e^2}{4\pi\epsilon_0 mc^2} \tag{2.44}$$

$$\sigma_e = \frac{8\pi}{3} r_e^2 \tag{2.45}$$

$$\sigma = \frac{8\pi}{3} r_e^2 \frac{\omega^4}{(\omega^2 - \omega_s^2)^2 + (\gamma\omega)^2} \tag{2.51}$$

$$f(\Delta\mathbf{k}, \omega) = \sum_{s=1}^{Z} \frac{\omega^2 e^{-i\Delta\mathbf{k}\cdot\Delta\mathbf{r}_s}}{\omega^2 - \omega_s^2 + i\gamma\omega} \tag{2.66}$$

$$f^0(\omega) = \sum_{s=1}^{Z} \frac{\omega^2}{\omega^2 - \omega_s^2 + i\gamma\omega} \tag{2.72}$$

In this chapter basics of electromagnetic theory are reviewed. Beginning with Maxwell's equations, the wave equation is developed and used to solve several problems of interest at short wavelengths. Poynting's theorem regarding the flow of electromagnetic energy is used to solve the power radiated by an accelerated electron. The concept of a scattering cross-section is introduced and applied to the scattering of radiation by free and bound electrons. A semiclassical model is used in the latter case. Scattering by a multi-electron atom is described in terms of a complex atomic scattering factor. Tabulated scattering factors, which are available in the literature for use in special circumstances, are described.

2.1 MAXWELL'S EQUATIONS AND THE WAVE EQUATION

In this chapter we will consider radiation and scattering by accelerated charges. We will use these results to study scattering cross-sections and interesting phenomena at visible, EUV, and

Chapter 3

WAVE PROPAGATION AND REFRACTIVE INDEX AT EUV AND SOFT X-RAY WAVELENGTHS

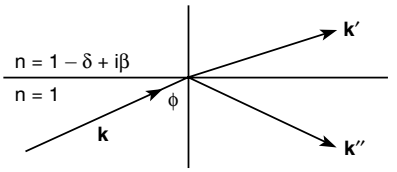

$$n(\omega) = 1 - \frac{n_a r_e \lambda^2}{2\pi}\left(f_1^0 - i f_2^0\right) \quad (3.9)$$

$$n(\omega) = 1 - \delta + i\beta \quad (3.12)$$

$$l_{\text{abs}} = \frac{\lambda}{4\pi\beta} \quad (3.22)$$

$$\sigma_{\text{abs.}} = 2 r_e \lambda f_2^0(\omega) \quad (3.28)$$

$$\Delta\phi = \left(\frac{2\pi\delta}{\lambda}\right)\Delta r \quad (3.29)$$

$$\theta_c = \sqrt{2\delta} \quad (3.41)$$

$$R_{s,\perp} \simeq \frac{\delta^2 + \beta^2}{4} \quad (3.50)$$

$$\phi_B \simeq \frac{\pi}{4} - \frac{\delta}{2} \quad (3.60)$$

In this chapter wave propagation in a medium of uniform atomic density is considered. Expressions for the induced motion of bound atomic electrons are used in combination with the wave equation to obtain the complex refractive index for EUV and soft x-ray propagation. This is then expressed in terms of the atomic scattering factors of Chapter 2. Phase velocity, absorption, reflection, and refraction are then considered. Results such as the total external reflection of x-rays at glancing incidence from the surface of a lossy material, the weak normal incidence reflection of x-rays, Brewster's angle, and Kramers–Kronig relations are obtained.

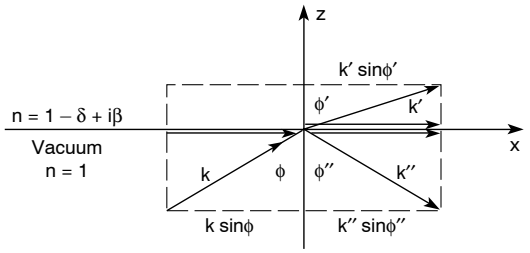

FIGURE 3.5. Parallel components of the wave vectors.

Since k and k'' propagate in vacuum, they are real and equal in magnitude as observed in Eq. (3.31); thus from (34b) we can write

$$\sin\phi = \sin\phi'' \tag{3.35a}$$

or

$$\boxed{\phi = \phi''} \tag{3.35b}$$

which states that *the angle of incidence equals the angle of reflection.* Considering the refracted wave $\mathbf{k}'$, Eq. (3.34b) permits us to write

$$k\sin\phi = k'\sin\phi' \tag{3.36}$$

Since both waves must oscillate at the same frequency (ω), we can write, by using Eq. (3.15), that

$$\omega = kc = k'c/n$$

or

$$k' = kn = \frac{\omega}{c}(1 - \delta + i\beta) \tag{3.37}$$

indicating that the propagation vector in the medium is complex, representing both phase variation and amplitude decay as the wave propagates, as seen previously in Eqs. (3.16) and (3.17). Equation (3.36) can now be rewritten as *Snell's law:*

$$\boxed{\sin\phi' = \frac{\sin\phi}{n}} \tag{3.38}$$

which formally describes the refractive turning of a wave entering a uniform, isotropic medium of complex refractive index n. The fact that n is complex implies that $\sin\phi'$ is also complex for real incidence angle ϕ. Thus both the wavevector k' and the turning angle ϕ', in the medium, have real and imaginary components, giving a somewhat more complicated representation of refraction and propagation.

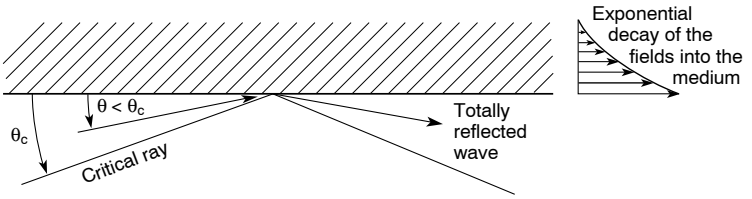

FIGURE 3.6. Glancing incidence radiation and total external reflection.

Snell's law (3.38) is valid over a wide range of wavelengths and photon energies. It is widely used in lens designs at visible wavelengths, and to describe such interesting phenomena as total internal reflection of visible light within the denser medium at water–air and glass–air interfaces. We will use Snell's law here to describe the near-total reflection of short wavelength radiation at glancing incidence to a material surface.

3.4 TOTAL EXTERNAL REFLECTION OF SOFT X-RAYS AND EUV RADIATION

For most angles of incidence the reflection coefficient for soft x-rays and extreme ultraviolet radiation is very small, as we will see in a following section of this chapter. This is due to the fact that the refractive index is very close to unity so that there is little change of field amplitudes across the interface. However, there is an important exception for radiation incident at a glancing angle to the material surface, far from the surface normal. We will see that in this case, radiation of any polarization experiences near total reflection. This *total external reflection* is widely used in experiments involving radiation transport, deflection, focusing, and filtering. Like its visible light counterpart total internal reflection (commonly observed in fish tanks and used for turning visible laser beams within glass prisms where the refractive index is greater than unity), the x-ray effect can be understood in large measure on the basis of Snell's law, Eq. (3.38). Snell's law indicates that visible light will be bent towards the surface normal ($\phi' < \phi$) when entering a medium of greater refractive index (n typically greater than 1.5 for glass or water at visible wavelengths). For EUV and x-rays, however, with the real part of the refractive index slightly less than unity, Snell's law indicates that the radiation is refracted in a direction slightly further from the surface normal. Inspection of Eq. (3.38) shows that for n slightly less than unity, $\sin\phi'$ is slightly larger than $\sin\phi$. Thus for near-glancing incidence (ϕ near $\pi/2$) the refraction angle ϕ' can equal $\pi/2$, indicating that to first order the refracted wave does not penetrate into the material, but rather propagates along the interface. In short order we will investigate the dependence of these fields on the parameters of the problem: the wavelength λ, incidence angle ϕ, and refractive index components δ and β. First, however, we consider the simplified problem with β approaching zero, which permits us to understand the basic phenomenon of total external reflection and quantify the critical angle with minimal mathematical complexity. The general effect is illustrated in Figure 3.6.

Considering Snell's law for a refractive index of $n \simeq 1 - \delta$, where for the moment we assume that β approaches zero, one has

$$\sin\phi' = \frac{\sin\phi}{1-\delta} \tag{3.39}$$

Thus the refracted wave is at an angle ϕ', somewhat further from the surface normal than ϕ

because of the $1 - \delta$ factor. As ϕ approaches $\pi/2$ it is evident that $\sin\phi'$ approaches unity somewhat faster. The limiting condition occurs at a *critical angle of incidence*, $\phi = \phi_c$, where $\phi' = \pi/2$, so that $\sin\phi' = 1$ and from Eq. (3.39)

$$\sin\phi_c = 1 - \delta \tag{3.40}$$

This is the condition for total external reflection; the incident x-rays do not penetrate the medium, but rather propagate along the interface at an angle $\phi' = \pi/2$. The angle for which this condition is just met is given by Eq. (3.40). Since $\delta \ll 1$ for x-rays, the phenomenon occurs only for glancing angles where ϕ is near 90°. Thus it is convenient to introduce the complimentary angle θ, measured from the interface as shown in Figure 3.6, where

$$\theta + \phi = 90^\circ$$

The critical angle condition (3.40) then becomes

$$\sin(90^\circ - \theta_c) = 1 - \delta$$

or

$$\cos\theta_c = 1 - \delta$$

Since $\delta \ll 1$ for x-rays, $\cos\theta_c$ is near unity, θ_c is very small, and we may make the small angle approximation

$$1 - \frac{\theta_c^2}{2} + \cdots = 1 - \delta$$

which has the solution

$$\boxed{\theta_c = \sqrt{2\delta}} \tag{3.41}$$

as the *critical angle for total external reflection of x-rays and extreme ultraviolet radiation*, a result first obtained by Compton[6] in 1922.

Since the real part of the refractive index can be written as [Eq. (3.13a)]

$$\delta = \frac{n_a r_e \lambda^2 f_1^0(\lambda)}{2\pi}$$

we have, to first order,

$$\theta_c = \sqrt{2\delta} = \sqrt{\frac{n_a r_e \lambda^2 f_1^0(\lambda)}{\pi}} \tag{3.42a}$$

Because the atomic density n_a, in atoms per unit volume, varies only slowly among the natural elements, the major functional dependencies of the critical angle are

$$\theta_c \propto \lambda\sqrt{Z} \tag{3.42b}$$

where we have used the fact that to first order f_1^0 is approximated by Z, although as we have seen f_1^0 is also a complicated function of wavelength (photon energy) for each element.

Chapter 4

MULTILAYER INTERFERENCE COATINGS

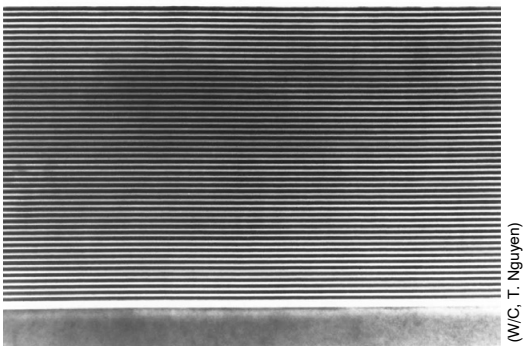

$$m\lambda = 2d \sin\theta$$

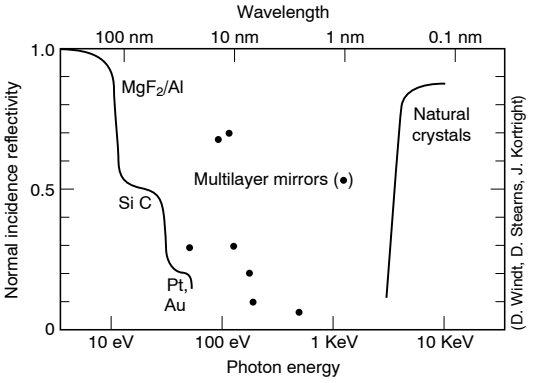

Multilayer interference coatings, often referred to as multilayer mirrors, are formed by depositing alternating layers of two materials of differing refractive index that form long-term stable interfaces. Typically the two materials are of alternating high and low atomic number (Z) in order to maximize the difference in electron density. The coatings permit the achievement of high normal incidence reflectivity, within a modest spectral bandwidth, at EUV wavelengths. They also offer new opportunities for glancing incidence reflectivity at soft x-ray and x-ray wavelengths. The coatings are largely amorphous (or to some degree polycrystalline) within individual layers, and reflection conforms to Bragg's law for a periodicity d equal to the thickness of one bilayer pair, typically measured in tens of atomic monolayers. Multilayer coatings have the great advantage of being adaptable to curved surfaces, enabling their use as reflective optics in EUV and soft x-ray microscopes, telescopes, and other applications.

4.1 INTRODUCTION

High reflectivity at normal incidence* can be achieved at EUV, and to some extent soft x-ray, wavelengths through the use of multilayer interference coatings, sometimes called reflection

*$\mathbf{k}$-vector perpendicular to the surface.

Chapter 5

SYNCHROTRON RADIATION

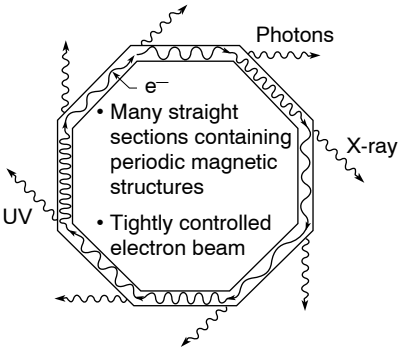

Bending Magnet:

$$\hbar\omega_c = \frac{3e\hbar B\gamma^2}{2m} \tag{5.7}$$

Wiggler:

$$\hbar\omega_c = \frac{3e\hbar B\gamma^2}{2m}$$

$$n_c = \frac{3K}{4}\left(1 + \frac{K^2}{2}\right)$$

$$P_T = \frac{\pi e K^2 \gamma^2 I N}{3\epsilon_0 \lambda_u}$$

Undulator:

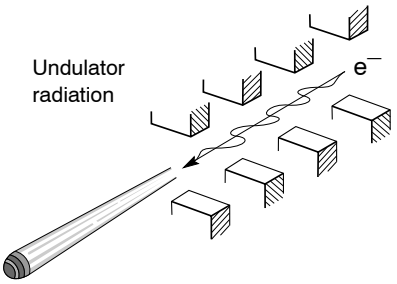

(see Colorplate X)

$$\lambda = \frac{\lambda_u}{2\gamma^2}\left(1 + \frac{K^2}{2} + \gamma^2\theta^2\right) \tag{5.28}$$

$$K = \frac{eB_0\lambda_u}{2\pi mc} \tag{5.18}$$

$$\theta_{\text{cen}} = \frac{1}{\gamma^*\sqrt{N}} \tag{5.15}$$

$$\left.\frac{\Delta\lambda}{\lambda}\right|_{\text{cen}} = \frac{1}{N} \tag{5.14}$$

$$\bar{P}_{\text{cen}} = \frac{\pi e\gamma^2 I}{\epsilon_0\lambda_u}\frac{K^2}{\left(1 + \frac{K^2}{2}\right)^2} f(K) \tag{5.41}$$

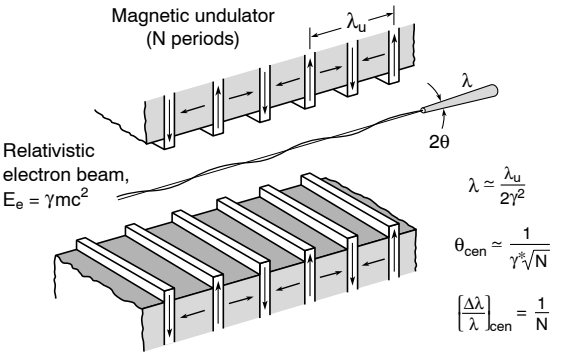

FIGURE 5.8. Illustration of narrow cone undulator radiation that is generated by electrons traversing a periodic magnet structure.

plane. The general polarization properties of bending magnet radiation for arbitrary angles of observations are discussed in Ref. 3.

5.3 CHARACTERISTICS OF UNDULATOR RADIATION

An electron traversing a periodic magnet structure[8] of moderate field strength will undergo a small amplitude oscillation and therefore radiate. If the electron's angular excursions are small compared to the natural radiation width, $\theta_e < 1/2\gamma$, the device is referred to as an *undulator* (see Figure 5.8). The resultant radiation is greatly reduced in wavelength, λ, from that of the magnet period, λ_u. We will see shortly that Lorentz contraction and relativistic Doppler shift lead to a reduction in the radiated wavelength by a factor of $2\gamma^2$. As γ can easily be several thousand, undulator periods measured in centimeters lead to observed x-ray wavelengths measured in angstroms.

While discussing undulator radiation, we will find it convenient to consider the radiation in several frames of reference. Many of the calculations will be done in the reference frame moving with the electron. We will then transform the results to the rest frame of the laboratory via Lorentz transformations (see Ref. 9 or Appendix F, Lorentz Space–Time Transformations). The following is a brief introduction to undulator radiation. A more detailed discussion will follow in subsequent sections.

In the frame moving with the electron, the electron "sees" a periodic magnet structure moving toward it with a relativistically (Lorentz) contracted period, λ', given by

$$\lambda' = \frac{\lambda_u}{\gamma} \tag{5.9}$$

where $\gamma \equiv 1/\sqrt{(1 - v^2/c^2)}$, v is the relative velocity, and c is the velocity of light in vacuum, as discussed in Appendix F. Due to the periodic magnet, the electron experiences an oscillation and consequently radiates. In the frame moving with the electron this problem is that of the classical *radiating dipole*, a point charge oscillating with an amplitude much smaller than the radiated wavelength. The frequency of this emitted radiation, in the reference frame of

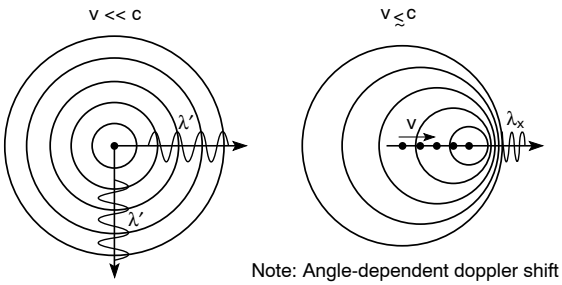

FIGURE 5.9. Radiation from an oscillating charge moving at (a) a non-relativistic and (b) a relativistic speed. Short wavelengths are observed because comparable speeds of the moving charge (v) and the radiation (c) reduce the separation of succeeding phase fronts. Indeed, as v approaches c, the spatial phase variations (λ) are dramatically compressed by many orders of magnitude. (Following J. Madey.)

the electron, is

$$f' = \frac{c}{\lambda'} = \frac{c\gamma}{\lambda_u}$$

To the observer in the fixed laboratory reference frame, the radiation wavelength is further reduced by Doppler shifting. The Doppler shift is dependent on the relative velocity and therefore is dependent on the observation angle θ, as can be deduced from Figure 5.9. The shortest wavelength is observed on axis. The relativistic form of the Doppler frequency formula is [see Appendix F, Eq. (F.8b)]

$$f = \frac{f'}{\gamma(1 - \beta\cos\theta)} = \frac{c}{\lambda_u(1 - \beta\cos\theta)} \tag{5.10}$$

where $\beta \equiv \mathrm{v}/c$ and θ is the observation angle measured from the direction of motion.

Let us first analyze the observed frequency on axis. Here $\theta = 0,\ \cos\theta = 1$, and

$$f = \frac{c}{\lambda_u(1 - \beta)}$$

As noted in Eq. (5.3), for $\beta \simeq 1$ we have $1 - \beta \simeq 1/2\gamma^2$. Therefore, the observed radiation frequency on axis is

$$f = \frac{2\gamma^2 c}{\lambda_u}$$

and the observed wavelength on axis is

$$\lambda = \frac{c}{f} = \frac{\lambda_u}{2\gamma^2} \tag{5.11}$$

Note that the observed wavelength, λ, is relativistically contracted by a factor $2\gamma^2$ from the period of the undulator. Again using the ALS as an example, with a 1.9 GeV electron energy, $\gamma \simeq 3700$ [see Eq. (5.5)]; thus $2\gamma^2 \simeq 2.8 \times 10^7$. If the undulator period is $\lambda_u = 5.0$ cm, the

resultant on-axis radiation will be relativistically shifted to an observed wavelength of order

$$\lambda \simeq \frac{5.0\text{cm}}{2.8 \times 10^7} \simeq 1.8\ \text{nm}$$

Thus the periodic magnet generates radiation peaked in the soft x-ray region of the electromagnetic spectrum.

If we wish to consider Doppler shifts at small angles off axis ($\theta \neq 0$), we can return to Eq. (5.10) and use the small angle approximation. The Taylor expansion for small angles is $\cos\theta = 1 - \theta^2/2 + \cdots$; therefore,

$$f = \frac{\frac{c}{\lambda_u}}{1 - \beta\left(1 - \frac{\theta^2}{2} + \cdots\right)} = \frac{\frac{c}{\lambda_u}}{1 - \beta + \frac{\beta\theta^2}{2} + \cdots} = \frac{\frac{c}{(1-\beta)\lambda_u}}{1 + \frac{\beta\theta^2}{2(1-\beta)}}$$

Since $\beta \simeq 1$ and by Eq. (3) $1 - \beta \simeq 1/2\gamma^2$, one has

$$f = \frac{\frac{2\gamma^2 c}{\lambda_u}}{1 + \frac{2\gamma^2\theta^2}{2} - \cdots} = \frac{2c\gamma^2}{\lambda_u(1 + \gamma^2\theta^2)}$$

In terms of the observed wavelength $\lambda = c/f$, one has to first order

$$\lambda = \frac{\lambda_u}{2\gamma^2}(1 + \gamma^2\theta^2) \tag{5.12}$$

We again see the $2\gamma^2$ contraction on axis, but now with the off-axis radiation having a wavelength increased by a factor $(1+\gamma^2\theta^2)$. Hence, to observe the narrow bandwidth characteristic of this relativistic harmonic oscillator, it is necessary to select only near-axis radiation.

As we will see explicitly in a following section, the magnetically induced undulation causes the electron to follow a somewhat longer pathlength as it traverses the undulator. Thus, the mean axial velocity is reduced, resulting in a modified Doppler shift and therefore somewhat longer wavelengths than indicated by Eq. (5.12), and a broader radiation cone as well.

5.3.1 Undulator Radiation Pattern

As we saw in Chapter 2, Eqs. (2.25)–(2.33), an oscillating electron of charge $-e$ undergoing an acceleration **a** will radiate electromagnetic waves characterized by an electric field (also see Leighton, Ref. 9).

$$E(\mathbf{r}, t) = \frac{ea(t - r/c)}{4\pi\epsilon_0 c^2 r}\sin\Theta$$

and an orthogonal magnetic field

$$H(\mathbf{r}, t) = \frac{ea(t - r/c)}{4\pi cr}\sin\Theta$$

where $t - r/c$ is the retarded time (delayed arrival at distance r), and Θ is the angle between the direction of acceleration (**a**) and the propagation direction ($\mathbf{k}_0$). Because the electric and magnetic fields are orthogonal, their cross product gives a Poynting vector **S** (power per

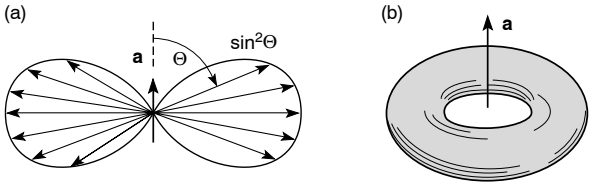

FIGURE 5.10. Illustration of an oscillating charge and the resultant radiation pattern. Note that there is no radiation in the direction of acceleration, giving the radiation pattern a doughnut-like appearance.

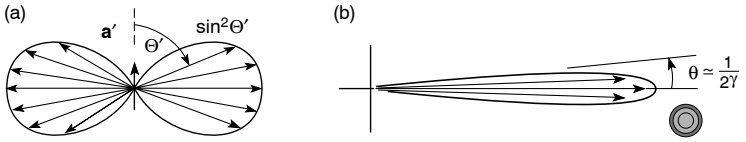

FIGURE 5.11 (see Colorplate VI). (a) Illustration of the radiation pattern of an oscillating electron in the frame of reference moving with the average electron speed. (b) Illustration of the radiation pattern of a highly relativistic electron as observed in the laboratory frame of reference. The shortest wavelengths are observed on axis. (Following Hofmann.[2])

unit area) of

$$\mathbf{S} = \mathbf{E} \times \mathbf{H} = \left[\frac{e^2 a^2 \sin^2 \Theta}{16\pi^2 \epsilon_0 c^3 r^2} \right] \mathbf{k}_0$$

The radiated power per unit solid angle is [Chapter 2, Eq. (2.34)]

$$\frac{dP}{d\Omega} = r^2 |\mathbf{S}| = \frac{e^2 a^2}{16\pi^2 \epsilon_0 c^3} \sin^2 \Theta$$

Hence, the radiation pattern has a toroidal $\sin^2 \Theta$ shape, because there is no radiation in the acceleration direction ($\Theta = 0$), as illustrated in Figure 5.10.

For an undulating electron, undergoing simple oscillations in its own reference frame (γ), one obtains the same radiation pattern. However, the radiation pattern as observed in the laboratory frame is relativistically contracted into a narrow radiation cone (the so-called searchlight effect) as shown in Figure 5.11(b). Considering the symmetry of the problem, it is convenient to work with a polar coordinate system measured from the z-axis. For instance, in the plane defined by the electron acceleration (**a**) and the z-axis, the factor $\sin^2 \Theta'$ becomes $\cos^2 \theta'$, θ' being the polar angle measured away from the z-axis in the primed coordinate system. In this primed electron frame of reference the radiation pattern has a half-intensity angle at $\cos^2 \theta' = \frac{1}{2}$ or $\theta' = 45^\circ$. According to Eq. (5.1), this corresponds to an angle in the unprimed laboratory (observer) frame of reference of $\theta \simeq 1/2\gamma$. Returning to the example of a 1.9 GeV electron ($\gamma \simeq 3700$), in this case traversing a periodic magnet structure, one anticipates that radiated x-rays will largely be confined to a cone of half angle 140 μrad. As we will see in the following paragraphs, further cone narrowing can be obtained in the case of undulator radiation.

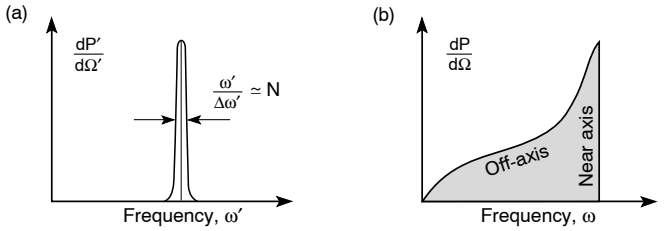

FIGURE 5.12. (a) The radiation spectrum as seen in the frame of reference moving with the electron is narrow with a relative spectral bandwidth of order $1/N$, where N is the number of oscillation periods. (b) In the laboratory frame of reference, the wavelengths are shorter, but the spectrum is broader due to off-axis Doppler effects. (Following Hofmann.[2])

5.3.2 The Central Radiation Cone

The spectrum of radiation in the two reference frames is shown in Figure 5.12(a) and (b). Figure 5.12(a) shows the narrow spectral width in the electron frame, set by the harmonic oscillation for a fixed number of periods N. This is essentially a frequency–time (Laplace) transform.

For example, the ALS has undulators of 5.0 cm period, with a length of 89 periods, so that one can expect $\Delta\omega'/\omega' = \Delta\lambda'/\lambda'$ of order 0.01. Note, however, that upon transformation to the laboratory frame of reference, off-axis Doppler effects will broaden this considerably. Figure 5.12(b) illustrates the Doppler shifted spectrum that results when the $\sin^2\Theta$ dipole radiation pattern is transformed according to Eqs. (5.1) and (5.12).

Recall that we have determined the undulator equation (5.12) in the laboratory frame, viz.,

$$\lambda \simeq \frac{\lambda_u}{2\gamma^2}(1 + \gamma^2\theta^2)$$

and have also noted that the radiation is primarily contained in a narrow cone of half angle $\theta = 1/2\gamma$. The corresponding spectral width within this cone can thus be estimated by taking the difference of Eq. (5.12) for two angles. Taking the wavelength as λ on axis ($\theta = 0$), and $\lambda + \Delta\lambda$ off axis at angle θ, then taking ratios, one obtains

$$\frac{\Delta\lambda}{\lambda} \simeq \gamma^2\theta^2 \tag{5.13}$$

where Eq. (5.13) shows how the wavelength increases as one observes the radiation off axis. Note that for radiation within the cone of half angle $\theta \simeq 1/2\gamma$ the relative spectral bandwidth given by Eq. (5.13) is $\frac{1}{4}$; thus the cone of half-intensity half angle encloses a relative spectral bandwidth of about 25%. Use of aperture spectral filtering is illustrated in Figure 5.13. Often, further spectral narrowing is desired, for instance, when probing in the vicinity of sharp atomic resonance features. In such cases, a monochromator of some type (see Chapter 8) is employed that acts as a narrow bandpass filter. In the case of radiation from a single electron or a tightly constrained bunch of electrons, modest spectral filtering (as narrow as $1/N$) can be obtained with a simple small-angle selecting aperture (pinhole). In this limit, we will see that angular width and spectral width are closely connected. The interrelationship is shown in Figure 5.14.

Further cone narrowing can be appreciated by considering the undulator equation for two angular positions, one on axis and one at angle θ, as we did previously in Eq. (5.13). If one

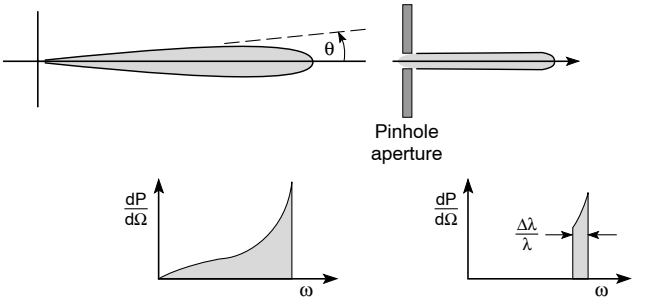

FIGURE 5.13. The spectrum of undulator radiation in the laboratory frame of reference before and after selecting an angular cone near the axis. With a sufficiently small electron beam phase space (size–angle product) this can provide a simple mechanism for monochromatization.

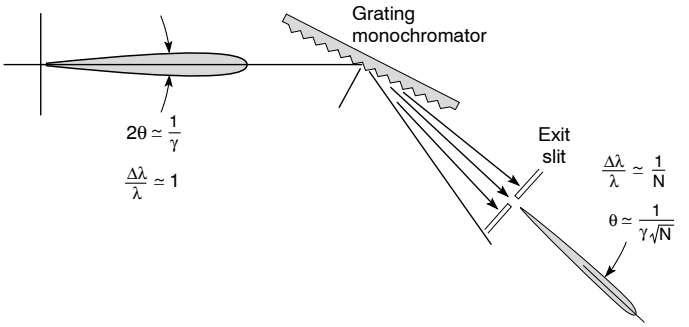

FIGURE 5.14. Illustration of a grating monochromator as used to filter undulator radiation to a "natural" spectral width $1/N$, and the concomitant cone narrowing to $1/\gamma\sqrt{N}$ that occurs with a tightly constrained electron beam.

sets the monochromator for a "natural" bandwidth $\Delta\lambda/\lambda$, set by the number of oscillation periods, N, then one obtains the condition

$$\boxed{\frac{\Delta\lambda}{\lambda} = \frac{1}{N}} \tag{5.14}$$

which, when combined with Eq. (5.13), indicates that narrower bandwidth radiation occurs in a *concomitantly narrower "central" radiation cone* of half width

$$\boxed{\theta_{\text{cen}} \simeq \frac{1}{\gamma\sqrt{N}}} \tag{5.15}$$

This narrow undulator radiation cone implies an emission solid angle reduced by a factor $1/N$. These factors become very important when considering brightness and coherence (see Chapter 8).

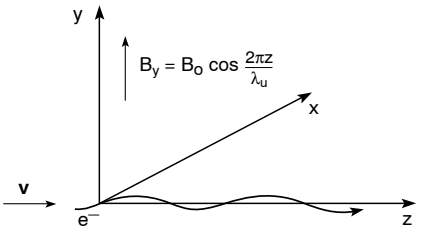

FIGURE 5.15. Electron motion in a periodic magnetic field.

The above analysis is for a single electron. For these results to hold for an electron beam with many electrons, it is necessary that all electrons in the bunch be contained within an angular variance of less than $1/\gamma\sqrt{N}$. This angular constraint on the electron beam is referred to as the *undulator condition*. Again considering 1.9 GeV electrons, with $\gamma \simeq 3720$ and $N \simeq 100$, one expects the 1% bandwidth radiation to be confined within a cone of angular half width $\theta \simeq 35\ \mu$rad.

5.4 UNDULATOR RADIATION: CALCULATIONS OF RADIATED POWER, BRIGHTNESS, AND HARMONICS

Having introduced the basic features of undulator radiation, we now wish to solve the problem by considering the equations of motion for a highly relativistic electron traversing a periodic magnetic field. In the laboratory frame, the electron experiences only the static, albeit periodic, magnetic field for small K. Hence, the laboratory is a convenient reference frame for the calculation. After calculating electron trajectories in the laboratory frame, we will transform to the frame of reference moving with the average electron motion (γ). Our next step will be to calculate the radiated fields in the electron frame where we have simple harmonic motion (dipole radiation). We will see a multiplicity of harmonics, $n\omega$, of this radiation. Finally, we will transform the radiated fields to the laboratory frame. The approach follows that of Hofmann.[2]

5.4.1 The Undulator Equation

The force equation for a charge in the presence of electric and magnetic fields can be written in any frame of reference as

$$\frac{d\mathbf{p}}{dt} = q(\mathbf{E} + \mathbf{v} \times \mathbf{B}) \tag{5.16}$$

where $\mathbf{p} = \gamma m\mathbf{v}$ is the momentum, q is the charge, $\mathbf{v}$ is the velocity, and $\mathbf{E}$ and $\mathbf{B}$ are the electric and magnetic fields, determined through Maxwell's equations. The problem we are considering is dominated by the applied dc magnetic field associated with a periodic magnet structure (undulator), as illustrated in Figure 5.15. There are no applied electric fields. Further, we consider the radiated electromagnetic fields due to the undulator radiation generated by many electrons to be relatively weak in the sense that the radiated fields have a negligible effect on the various electron motions. To this level of approximation, we take $\mathbf{E} \simeq 0$ in Eq. (5.16). Note that this would not be the case in a sufficiently long undulator. In fact, the effect of the radiated fields would lead to free electron laser (FEL) action.[10, 11] With these

approximations the momentum equation becomes

$$\frac{d\mathbf{p}}{dt} = -e(\mathbf{v} \times \mathbf{B})$$

For the undulator case with relatively weak radiated fields (pre-FEL action), we take the approximations $E \simeq 0$ and $\mathbf{B}_y = \mathbf{B}_0 \cos(2\pi z/\lambda_u)$ plus a negligible radiation field. Additionally, taking to first order $\mathbf{v} \simeq \mathbf{v}_z$, the vector components in the x-direction give

$$m\gamma \frac{d\mathrm{v}_x}{dt} = +e\mathrm{v}_z B_y$$

$$m\gamma \frac{d\mathrm{v}_x}{dt} = e\frac{dz}{dt} \cdot B_0 \cos\left(\frac{2\pi z}{\lambda_u}\right) \qquad (0 \le z \le N\lambda_u)$$

Now we can solve for the transverse oscillation v_x. This gives rise to the primary source of undulator radiation. To first order, we will find v_x as a function of axial position z. Continuing the algebra,

$$m\gamma \, d\mathrm{v}_x = e \, dz \, B_0 \cos\left(\frac{2\pi z}{\lambda_u}\right)$$

Integrating both sides gives

$$m\gamma \mathrm{v}_x = eB_0 \frac{\lambda_u}{2\pi} \int \cos\left(\frac{2\pi z}{\lambda_u}\right) \cdot d\left(\frac{2\pi z}{\lambda_u}\right)$$

or

$$m\gamma \mathrm{v}_x = \frac{eB_0\lambda_u}{2\pi} \sin\left(\frac{2\pi z}{\lambda_u}\right) \tag{5.17}$$

This is an exact solution of the simplified equation of motion, but note that z is not a linear function of time. That is, v_z is not constant, but rather involves oscillations itself. Hence, terms of the $\sin(\cdots \sin)$ type will appear, giving rise to harmonics.

Define the non-dimensional magnetic strength for a periodic magnet parameter as[12]

$$\boxed{K \equiv \frac{eB_0\lambda_u}{2\pi mc}} \tag{5.18a}$$

or, in convenient units,

$$K = 0.9337 B_0(\mathrm{T})\lambda_u(\mathrm{cm}) \tag{5.18b}$$

The electron's transverse velocity can then be written as

$$\mathrm{v}_x = \frac{Kc}{\gamma} \sin\left(\frac{2\pi z}{\lambda_u}\right) \tag{5.19}$$

Note that the angle the electron motion makes with the z-axis is a sine function bounded

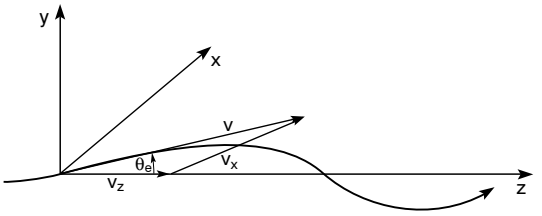

FIGURE 5.16. Electron angular excursions are harmonic, with maximum excursion K/γ. For $K < 1$ the angular excursions are within the natural radiation cone $(1/2\gamma)$, leading to interesting interference effects that are manifested in cone narrowing, higher spectral brightness, and in some cases partial coherence. The case of small angular excursions ($K < 1$) is referred to as the undulator limit. For $K \gg 1$ such interference effects are not possible. This limit ($K \gg 1$) is referred to as the wiggler limit. The scales here are exaggerated in the x-direction for clarity of presentation.

by $\pm K/\gamma$, i.e.,

$$\tan\theta_e = \frac{\mathrm{v}_x}{\mathrm{v}_z} \simeq \frac{K}{\gamma}\sin\left(\frac{2\pi z}{\lambda_u}\right) \tag{5.20}$$

so that K is also referred to as the (magnetic) *deflection parameter*. Note that to good approximation we have taken $\mathrm{v}_z \simeq c$. Thus the maximum excursion angle (see Figure 5.16) is

$$|\theta_{e,\,\max}| \simeq \frac{K}{\gamma} \tag{5.21}$$

This is the root of differences between undulator radiation and wiggler radiation. Recall that the characteristic half angle for emission of radiation is $\theta_{\mathrm{rad}} \simeq 1/2\gamma$. Thus, for magnet strength characterized by $K \leq 1$, the electron angular excursions lie within the radiation cone. This is the undulator case where interesting interference effects can occur, narrow bandwidths result, and narrower radiation cones are obtained.

In the strong field case, $K \gg 1$, we refer to *wiggler radiation*. In this case, interference opportunities are lost because the radiation from various segments of an oscillation are widely separated in angle and therefore do not overlap in space after some propagation distance. Nonetheless, other valuable attributes appear. Primarily, wiggler radiation provides a $2N$ increase in radiated power and a broad shift to higher photon energies. We will discuss both cases ($K < 1$, $K \gg 1$) further.

Recall that Eq. (5.19) is not that of a simple time harmonic, because $z = z(t)$ is only approximately equal to ct. To see this explicitly, we recall that γ is constant in a magnetic field; thus for motion in the x, z-plane ($\mathrm{v}_y = 0$),

$$\gamma \equiv \frac{1}{\sqrt{1-\frac{\mathrm{v}^2}{c^2}}} = \frac{1}{\sqrt{1-\frac{\mathrm{v}_x^2+\mathrm{v}_z^2}{c^2}}}$$

Thus,

$$\frac{\mathrm{v}_z^2}{c^2} = 1 - \frac{1}{\gamma^2} - \frac{\mathrm{v}_x^2}{c^2} \tag{5.22}$$

Knowing v_x from Eq. (5.19), we can solve for v_z:

$$\frac{v_z^2}{c^2} = 1 - \frac{1}{\gamma^2} - \frac{K^2}{\gamma^2}\sin^2\left(\frac{2\pi z}{\lambda_u}\right)$$

To first order in the small parameter K/γ,

$$\frac{v_z}{c} = 1 - \frac{1}{2\gamma^2} - \frac{K^2}{2\gamma^2}\sin^2\left(\frac{2\pi z}{\lambda_u}\right) \tag{5.23a}$$

where $\sin^2 k_u z = \frac{1}{2}(1 - \cos 2k_u z)$, and thus

$$\frac{v_z}{c} = 1 - \frac{1 + K^2/2}{2\gamma^2} + \frac{K^2}{4\gamma^2}\cos 2k_u z \tag{5.23b}$$

Hence, the axial velocity (z-direction) has a reduced average component and a component oscillating at twice the magnet spatial frequency. By averaging over a single period, we can determine the average axial velocity, which plays a major role in the relativistic transformations. Defining an average quantity

$$\bar{v}_z \equiv \frac{L}{T} = \frac{L}{\int_0^L dz/v_z} \tag{5.24}$$

where v_z is given in Eq. (5.23b) and where T is the time required for the electron to travel a distance $L = N\lambda_u$. Then

$$\bar{v}_z = c\left[1 - \frac{1 + K^2/2}{2\gamma^2}\right]\left[\frac{L}{\int_0^L \frac{dz}{1+\alpha\cos 2k_u z}}\right]$$

where

$$\alpha = \frac{K^2}{4\gamma^2\left[1 - \frac{1+K^2/2}{2\gamma^2}\right]}$$

Expanding the denominator of the integral to second order in the small parameter α, one obtains

$$\bar{v}_z = c\left[1 - \frac{1 + K^2/2}{2\gamma^2}\right]\left(1 - \frac{\alpha^2}{2}\right)$$

where the α^2 term is of order $1/\gamma^4$ and thus can be ignored, so that the average axial velocity at finite K is given by

$$\frac{\bar{v}_z}{c} = 1 - \frac{1 + K^2/2}{2\gamma^2} \tag{5.25}$$

From this, we can define an effective axial value of the relativistic factor,

$$\boxed{\gamma^* \equiv \frac{\gamma}{\sqrt{1 + K^2/2}}} \tag{5.26}$$

where the asterisk (*) refers to the reduction of the relativistic contraction factor by an amount $\sqrt{1 + K^2/2}$. Hence Eq. (5.25) can be rewritten as

$$\frac{\bar{v}_z}{c} = 1 - \frac{1}{2\gamma^{*2}} \tag{5.27}$$

As a consequence, the observed wavelength in the laboratory frame of reference is modified from that given in Eq. (5.12), now taking the form

$$\lambda = \frac{\lambda_u}{2\gamma^{*2}}(1 + \gamma^{*2}\theta^2)$$

that is, the Lorentz contraction and relativistic Doppler shift now involve γ^* rather than γ. Expanding γ^* according to Eq. (5.26), one has

$$\lambda = \frac{\lambda_u}{2\gamma^2}\left(1 + \frac{K^2}{2}\right)\left(1 + \frac{\gamma^2}{1 + K^2/2}\theta^2\right)$$

or

$$\boxed{\lambda = \frac{\lambda_u}{2\gamma^2}\left(1 + \frac{K^2}{2} + \gamma^2\theta^2\right)} \tag{5.28}$$

where we recall that $K \equiv eB_0\lambda_u/2\pi mc$. Equation (5.28) is the *undulator equation*, which describes the generation of short (x-ray) wavelengths through the factor $\lambda_u/2\gamma^2$, magnetic tuning through $K^2/2$, and off-axis wavelength variations through $\gamma^2\theta^2$. Note that wavelength tuning through variations of K requires changing the magnet gap. This is more desirable than γ-tuning, as it affects only the desired experimental station on a multi-undulator storage ring (see Figure 5.5). In practical units the wavelength λ and corresponding photon energy $E = 2\pi\hbar c/\lambda$ are given by

$$\lambda(\text{nm}) = \frac{1.306\lambda_u(\text{cm})\left(1 + \frac{K^2}{2} + \gamma^2\theta^2\right)}{E_e^2(\text{GeV})} \tag{5.29a}$$

and

$$E(\text{keV}) = \frac{0.9496E_e^2(\text{GeV})}{\lambda_u(\text{cm})\left(1 + \frac{K^2}{2} + \gamma^2\theta^2\right)} \tag{5.29b}$$

where λ_u is to be given in centimeters and the electron energy E_e in GeV.

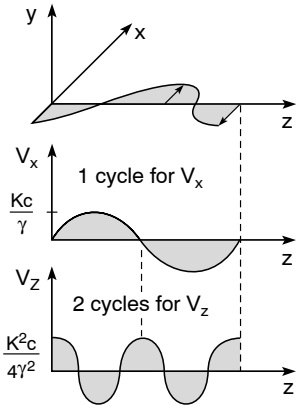

FIGURE 5.17. Illustration of the first and second harmonic motions of the electron.

5.4.2 Comments on Undulator Harmonics

In addition to modifying the observed wavelength of the fundamental [as given by Eq. (5.28)], the effect of transverse oscillations introduces higher harmonics into the motion. We will see that the harmonic amplitudes scale as K^n, where n is the harmonic number. These higher harmonics of the radiation will occur at frequencies $n\omega_1$ and wavelengths λ_1/n. Because short wavelengths are difficult to generate, harmonics are of great interest, especially since they are a natural consequence of the motion. Harmonics are frequently used to extend the photon energy range of a given undulator or facility.

We begin by considering second harmonic motion. From Eq. (23b) – repeated below – we have

$$\frac{v_z}{c} = 1 - \frac{1 + K^2/2}{2\gamma^2} + \frac{K^2}{4\gamma^2}\cos\left(2 \cdot \frac{2\pi z}{\lambda_u}\right)$$

This expression displays both the decreased axial velocity and an axial velocity modulation at twice the fundamental frequency. This is referred to as a second harmonic of the motion and is illustrated in Figure 5.17. If the first order (fundamental) motion leads to radiation at frequency ω_1' in the electron frame, then the axial harmonic will radiate at $\omega_2' = 2\omega_1'$; hence, it is called *second harmonic* radiation. Note that the magnitude of the second harmonic term scales as K^2.

Note that the second harmonic oscillations of the electron are at right angles to the fundamental oscillations. That is, the fundamental radiation results from oscillations in the x-direction, while the second harmonic (and other even harmonics) result from oscillations in the z-direction. As a result, the polarization is different. Additionally, when transformed to the laboratory frame, the angular distributions will be different. Figure 5.18 illustrates the radiation patterns of the fundamental and second harmonics.

If we further analyze details of the electron motion, we will find that for larger K-values, $K \geq 1$, additional harmonics will appear due to the continued mixing of harmonic motions. As K increases, this mixing will eventually lead to a strongly non-sinusoidal *wiggler limit*. In all cases, the observed wavelengths will be governed by an extension of the undulator equation:

$$\lambda_n = \frac{\lambda_u}{2\gamma^2 n}\left(1 + \frac{K^2}{2} + \gamma^2\theta^2\right) \tag{5.30}$$

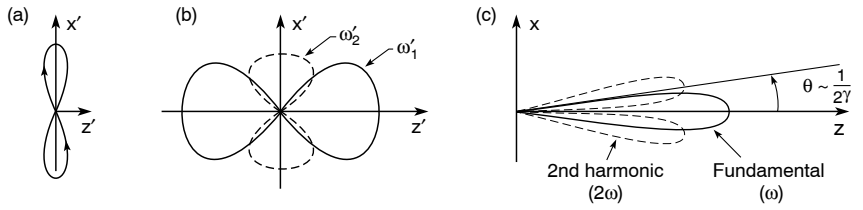

FIGURE 5.18. (a) Illustration of the figure eight electron motion in the frame of reference moving with the average electron velocity, and the resultant radiation patterns at the fundamental and second harmonic frequencies in both (b) the frame of reference moving with the electron and (c) the laboratory frame of reference.

Due to the increased number of cycles, the relative spectral bandwidth is also improved,[†] viz.,

$$\left(\frac{\Delta\lambda}{\lambda}\right)_n = \frac{1}{nN} \tag{5.31}$$

where n is the harmonic number and N is the number of magnetic periods.

From Figure 5.18, we see that the even harmonics radiate a pattern that peaks off axis and has zero intensity on axis. (Note that within a full electron bunch, this will be modified due to random individual motions slightly off axis, i.e., to finite phase space effects.) As a consequence, the even harmonics tend to be relatively weak on axis and, upon transformation to the laboratory frame, radiate into a hollow cone of radiation. We will see later that this cone has less interesting coherence and brightness properties. On the other hand, the odd harmonics ($n = 1, 3, 5, \ldots$) radiate on axis with a narrow spectrum and into a narrow forward cone. Hence, they are quite interesting as sources of high brightness and partially coherent x-rays. We will return to this subject in Section 5.5.

5.4.3 Power Radiated in the Central Radiation Cone

The undulator equation (5.28) tells us the wavelength of radiation as a function of magnet period λ_u, magnet deflection parameter K, electron energy γ (in rest energy units), and polar angle of observation θ. Now we would like to calculate the amount of power radiated. A natural and interesting choice is to calculate the power radiated into the central radiation cone, of half angle θ_{cen}, which we can identify with a relative spectral bandwidth $\lambda/\Delta\lambda \simeq N$, where N is the number of magnetic periods and thus the number of oscillations the electron executes in traversing the undulator. This has a natural appeal, common to our experience with other physical phenomena involving oscillators, gratings, etc., which we embody mathematically in our time–frequency and space–angle transformations. The choice of a central radiation cone containing the $1/N$ relative spectral bandwidth is also interesting because applications of undulator radiation generally involve the use of narrow bandwidth, quasi-monochromatic radiation, and the $1/N$ bandwidth is as small[‡] as one can obtain without use of a monochromator.

[†] In practice this narrowed spectral bandwidth is limited to the first few harmonics due to electron energy spread ($\Delta\gamma$) in a many-electron beam. Typically $\Delta\gamma/\gamma$ is of order 10^{-3} in a modern storage ring.

[‡] In fact the $1/N$ value is idealistic in that in practice one utilizes radiation from a multi-electron bunch for which there is an angular divergence due to the slightly varying electron trajectories. In specific cases considered later in this chapter, this typically contributes an additional broadening to the relative spectral bandwidth.

In Section 5.3.3 we used a simplified version of the undulator equation to introduce the concept of a central radiation cone, finding that for a bandwidth $1/N$ the cone half angle is $1/\gamma\sqrt{N}$. Having reconsidered electron motion in an undulator of finite K (Section 5.4.1), we can now follow the same arguments using the corrected undulator equation (5.28), viz.,

$$\lambda = \frac{\lambda_u}{2\gamma^2}\left(1 + \frac{K^2}{2} + \gamma^2\theta^2\right)$$

Writing this equation twice, once for a wavelength λ_0 corresponding to $\theta = 0$, and once for an off-axis angle θ_{cen} such that it encompasses a full bandwidth $\Delta\lambda$, subtracting the two equations and normalizing (as was done in Section 5.3.2, but now for finite K), one obtains a corrected formula for the central radiation cone

$$\boxed{\theta_{\text{cen}} = \frac{1}{\gamma^*\sqrt{N}} = \frac{\sqrt{1 + K^2/2}}{\gamma\sqrt{N}}} \tag{5.32}$$

of a single electron, containing a relative spectral bandwidth $\Delta\lambda/\lambda = 1/N$, where $\gamma^* = \gamma/\sqrt{1 + K^2/2}$, as defined earlier in Eq. (5.26). Thus for finite K there are not only longer wavelengths at each angle, but also an enlargement of the central radiation cone. We can trace both effects to the reduced average axial velocity of the electron for finite K, and thus to reduced effects of the angle dependent relativistic Doppler shift. A further discussion of spectral bandwidth is presented in Section 5.4.4.

Our task now is to calculate the power radiated within the central cone, at the fundamental frequency only. In later sections we will calculate other details, including the total power radiated. Our approach will be to use our knowledge of classical dipole radiation, as considered earlier in Chapter 2. We might ask how this can be done in a situation involving highly relativistic motion. The technique is to transfer the calculation to the frame of reference moving with the average electron velocity. In this frame of reference the electron motion is non-relativistic, at least for modest K, and the oscillation amplitude is small compared to the wavelength (in the frame of reference in which the calculation is made), as it should be for the dipole approximation to be valid. Having the desired power calculations, the results are then Lorentz transformed back to the laboratory (observer) frame of reference using straightforward but relativistically correct angular relationships given in Appendix F. This procedure gives us maximum leverage on the use of classical radiation results, and provides very valuable insights to the most important properties of undulator radiation. The process is outlined in Table 5.4.

Following the procedure outlined in Table 5.4, the electron velocity in the laboratory frame of reference has been derived, from Newton's second law of motion, as Eq. (5.19),

$$\mathrm{v}_x = \frac{Kc}{\gamma}\sin\frac{2\pi z}{\lambda_u}$$

which we can write as

$$\mathrm{v}_x = \frac{Kc}{\gamma}\sin k_u z$$

To obtain the acceleration we need v_x as a function of time. To first order we assume that

TABLE 5.4. An outline of the procedure for calculating power radiated by relativistic electrons traversing a periodic undulator. Electron motion is determined in the laboratory frame of reference. A Lorentz transformation to the frame of reference moving with the average electron velocity permits the use of classical dipole radiation (Chapter 2), as the electron motion is non-relativistic in this frame. The dipole radiation results are then Lorentz transformed back to the laboratory frame of reference.

x, z, t laboratory frame of reference

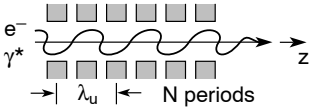

Determine x, z, t motion:

$$\frac{d\mathrm{p}}{dt} = -e\,(\mathbf{E} + \mathbf{v}\times\mathbf{B})$$

$$m\gamma\frac{dv_x}{dt} = e\,\frac{dz}{dt}B_0\cos\frac{2\pi z}{\lambda_u}$$

$$\mathrm{v}_x(t);\ a_x(t) = \cdots$$

$$\mathrm{v}_z(t);\ a_z(t) = \cdots$$

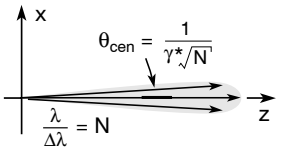

$$\frac{dP}{d\Omega} = 8\gamma^{*2}\frac{dP'}{d\Omega'}$$

$$\frac{d\bar{P}}{d\Omega} = \frac{e^2\,c\gamma^4}{\epsilon_0\lambda_u^2}\,\frac{K^2}{[1+K^2/2]^3}\begin{cases}K\le 1\\ \theta\le\theta_{\mathrm{cen}}\end{cases}$$

$$\Delta\Omega_{\mathrm{cen}} = \pi\theta_{\mathrm{cen}}^2 = \pi/\gamma^{*2}N$$

$$\bar{P}_{\mathrm{cen}} = \frac{\pi e^2 c\gamma^2}{\epsilon_0\lambda_u^2 N}\,\frac{K^2}{[1+K^2/2]^2}$$

N_e uncorrelated electrons:

$$N_e = IL/ec,\ L = N\lambda_u$$

$$\bar{P}_{\mathrm{cen}} = \frac{\pi e\gamma^2 I}{\epsilon_0\lambda_u}\,\frac{K^2}{[1+K^2/2]^2}$$

x', z', t' frame of reference moving with the average velocity of the electron

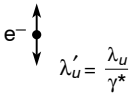

x', z', t' motion
$a'(t')$ acceleration

Dipole radiation:

$$\frac{dP'}{d\Omega'} = \frac{e^2 a'^2\sin^2\Theta'}{16\pi^2\epsilon_0 c^3}$$

$$\frac{dP'}{d\Omega'} = \frac{e^2 c\gamma^2}{4\epsilon_0\lambda_u^2}\,\frac{K^2}{[1+K^2/2]^2}(1-\sin^2\theta'\cos^2\phi')\cos^2\omega'_u t'$$

Lorentz transformation

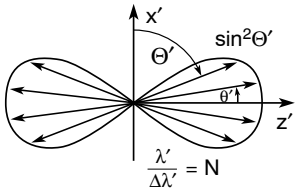

$z \simeq \bar{\mathrm{v}}_z t = \beta^* ct$, where $\bar{\mathrm{v}}_z$ is the average electron velocity in the z-direction and β^* is very close to unity. The velocity can then be written as

$$\mathrm{v}_x \simeq \frac{Kc}{\gamma}\sin k_u\beta^* ct = \frac{Kc}{\gamma}\sin\omega_u t$$

22. H. Onuki, "Elliptically Polarized Synchrotron Radiation Source with Crossed and Retarded Magnetic Fields," *Nucl. Instrum. and Meth. A 246*, 94 (1986).
23. H. Onuki, N. Saito, and T. Saito, "Undulator Generating any Kind of Elliptically Polarized Radiation," *Appl. Phys. Lett. 52*, 173 (1988).
24. P. Elleaume, "A Flexible Planar/Helical Undulator Design for Synchrotron Sources," *Nucl. Instrum. and Meth. A 291*, 371 (1990).
25. B. Di Viacco and R.P. Walker, "Fields and Trajectories in Some New Types of Permanent Magnet Helical Undulators," *Nucl. Instrum. Meth. A 292*, 517 (1990).
26. S. Sasaki, K. Kakunori, T. Takada, T. Shimada, K. Yanagida, and Y. Miyahara, "Design of a New Type of Planar Undulator for Generating Variably Polarized Radiation," *Nucl. Instrum. Meth. A 331*, 763 (1993).
27. S. Sasaki,"Analysis for a Planar Variably-Polarizing Undulator," *Nucl. Instrum. and Meth. A347*, 83 (1994).
28. R. Carr and S. Lidia, "The Adjustable Phase Planar Helical Undulator," *Proc. SPIE 2013*, 56 (1993); S. Lidia and R. Carr, "An Elliptically Polarizing Undulator with Phase Adjustable Polarization and Energy," *Nucl. Instrum. and Meth. A 347*, 77 (1994); R. Carr, J.B. Kortright, M. Rice, and S. Lidia, "Performance of the Elliptically Polarizing Undulator at SPEAR," *Rev. Sci. Instrum. 66*, 1862 (1995).
29. S. Marks, C. Cortopassi, J. De Vries, E. Hoyer, R. Leinbach, Y. Minamihara, H. Padmore, P. Pipersky, D. Plate, R. Schlueter, and A. Young, "Advanced Light Source Elliptically Polarizing Undulator," *Proc. 1997 Particle Accelerator Conference (1998)*, p. 3221; A. Young, V. Martynov, and H. Padmore, "An Elliptically Polarizing Undulator Beamline at the Advanced Light Source," *J. Electr. Spectr.* (to be published, 1999).
30. H. Kitamura, "Present Status of SPring-8 Insertion Devices," *J. Synchr. Rad. 5*, 184 (1998).
31. E. Gluskin, "APS Insertion Devices: Recent Developments and Results," *J. Synchr. Rad. 5*, 189 (1998).
32. J. Chavanne, P. Elleaume, and P. van Vaerenbergh, "The ESRF Insertion Devices," *J. Synchr. Rad. 5*, 196 (1998).
33. E.P. Ippen, C.V. Shank, and A. Dienes, "Passive Mode Locking of the CW Dye Laseer," *Appl. Phys. Lett. 21*, 348 (1972); R.L. Fork, B.I. Greene, and C.V. Shank, "Generation of Optical Pulses Shorter than 0.1 psec by Colliding Pulse Mode Locking," *Appl. Phys. Lett. 38*, 671 (1981).
34. C. Pellegrini, J. Rosenzweig, G. Travish, K. Bane, R. Boyce, G. Loew, P. Morton, H.-D. Nuhn, J. Paterson, P. Pianetta, T. Raubenheimer, J. Seeman, R. Tatchyn, V. Vylet, H. Winick, K. Halbach, K.-J. Kim, M. Xie, D. Prosnitz, E.T. Scharlemann, R. Bonifacio, L. De Salvo, and P. Pierini, "The SLAC Soft X-Ray High Power FEL," *Nucl. Instrum. Meth. A 341*, 326 (1994).
35. G.N. Kulipanov, A.N. Skrinsky, and N.A. Vinokurov, "Synchrotron Light Sources and Recent Developments of Accelerator Technology," *J. Synchr. Rad. 5*, 176 (1998).
36. K.-J. Kim, "Advanced Capabilities for Future Light Sources," *J. Synchr. Rad. 5*, 202 (1998).
37. R.W. Schoenlein, W.P. Leemans, A.H. Chin, P. Volfbeyn, T.E. Glover, P. Balling, M.S Zolotorev, K.-J. Kim, S. Chattopadhyay, and C.V. Shank, "Femtosecond X-Ray Pulses at 0.4 Å Generated by 90° Thomson Scattering: A Tool for Probing the Structural Dynamics of Materials," *Science 274*, 236 (11 October 1996).
38. W.P. Leemans, R.W. Schoenlein, P. Volfbeyn, A.H. Chin, T.E. Glover, P. Balling, M.S Zolotorev, K.-J. Kim, S. Chattopadhyay, and C.V. Shank, "Interaction of Relativistic Electrons with Ultrashort Laser Pulses: Generation of Femtosecond X-Rays and Microprobing of Electronbeams," *IEEE J. Quant. Electr. 33*, 1925 (1997); W.P. Leemans et al., "X-Ray Based Subpicosecond Electron Bunch Characterization Using 90° Thomson Scattering," *Phys. Rev. Lett. 77*, 4182 (1996).
39. K.-J. Kim, S. Chattopadhyay, and C.V. Shank, "Generation of Femtosecond X-Rays by 90° Thomson Scattering," *Nucl. Instrum. Meth. A 341*, 351 (1994).
40. A.H. Chin, R.W. Schoenlein, T.E. Glover, P. Balling, W.P. Leemans, and C.V. Shank, "Ultrafast Structural Dynamics in InSb Probed by Time-Resolved X-Ray Diffraction," *Phys. Rev. Lett.* (to be published, 1999); A.H. Chin, "Ultrashort X-Ray Pulse Science," Ph.D. thesis, Physics Department, University of California, Berkeley (1998).
41. A.A. Zholents and M.S. Zolotorev, "Femtosecond X-Ray Pulses of Synchrotron Radiation," *Phys. Rev. Lett. 76*, 912 (1996).

Chapter 7

EXTREME ULTRAVIOLET AND SOFT X-RAY LASERS

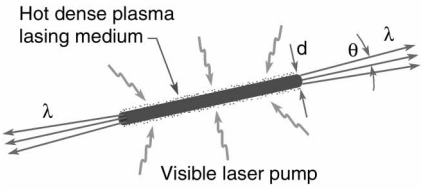

(see Colorplate XII)

$$\frac{I}{I_0} = e^{GL} \tag{7.2}$$

$$G = n_u \sigma_{\text{stim}} F \tag{7.4}$$

$$\sigma_{\text{stim}} = \frac{\pi \lambda r_e}{(\Delta\lambda/\lambda)} \left(\frac{g_l}{g_u}\right) f_{lu} \tag{7.18}$$

$$\frac{P}{A} = \frac{16\pi^2 c^2 \hbar (\Delta\lambda/\lambda) GL}{\lambda^4} \tag{7.22}$$

Lasing at short wavelengths in the EUV and soft x-ray regions of the spectrum is achieved in hot dense plasmas. Temperatures of several hundred electron volts to above 1 keV are required to collisionally excite atoms (ions) to the required energy levels. As these are well above the binding energies of outer electrons, the atoms are necessarily ionized to a high degree. Upper state lifetimes are typically measured in picoseconds, so that energy delivery (pumping) must be fast. As a result high power infrared, visible, and ultraviolet lasers are generally employed to create and heat the plasma, although in some cases fast electrical discharges are employed. Population inversion is generally accomplished through selective depopulation, rather than selective population. High gain lasing requires a high density of excited state ions, thus mandating a high density plasma. Preferred electron configurations are hydrogen-like (single electron, nuclear charge $+Ze$), neon-like (10 electrons), and nickel-like (28 electrons) ions, which tend to have a large fraction of the plasma ions in a desired ionization state. The short lifetime of hot dense plasmas limits the effectiveness of cavity end mirrors, so that in general these are high gain single pass lasers, albeit with some exceptions. Lacking multipass mode control, short wavelength lasers typically are far from diffraction limited. Temporal coherence lengths, set largely by ion Doppler line broadening, are typically 10^4 waves. The pumping power necessary to produce short wavelength lasers scales as $1/\lambda^4$. Recent high gain experiments demonstrate a capability for saturated lasing throughout much of this spectral region.

Chapter 8

COHERENCE AT SHORT WAVELENGTHS

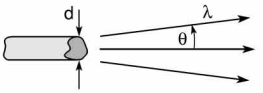

$$l_{\mathrm{coh}} = \lambda^2/(2\,\Delta\lambda) \text{ [temporal (longitudinal) coherence]} \tag{8.3}$$

$$d \cdot \theta = \lambda/2\pi \text{ [spatial (transverse) coherence]} \tag{8.5}$$

$$\text{or } d \cdot 2\theta\big|_{\mathrm{FWHM}} = 0.44\,\lambda \tag{8.5*}$$

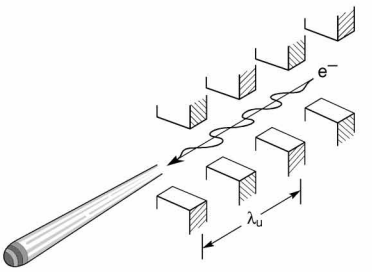

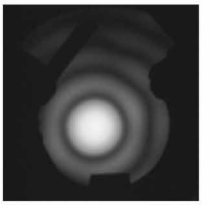

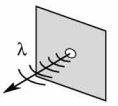

$$\bar{P}_{\mathrm{coh},N} = \frac{(\lambda/2\pi)^2}{(d_x\theta_x)(d_y\theta_y)}\,\bar{P}_{\mathrm{cen}} \tag{8.6}$$

$$\bar{P}_{\mathrm{coh},\lambda/\Delta\lambda} = \frac{e\lambda_u I\eta(\Delta\lambda/\lambda)N^2}{8\pi\epsilon_0 d_x d_y} \cdot \left\{1 - \frac{\hbar\omega}{\hbar\omega_0}\right\} f(K) \tag{8.9}$$

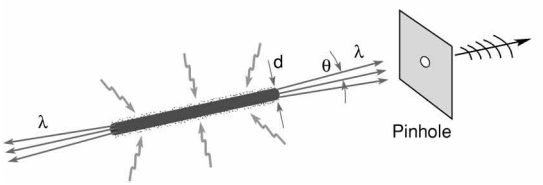

$$P_{\mathrm{coh}} = \frac{(\lambda/2\pi)^2}{(d_x\theta_x)(d_y\theta_y)}\,P_{\mathrm{laser}} \tag{8.11}$$

Whereas spatially and temporally coherent radiation is plentiful at visible wavelengths due to the availability of lasers, it is just becoming available at shorter wavelengths. In this chapter we review the concepts of spatial and temporal coherence, some applications that require radiation with these properties, and methods to generate spatially and spectrally filtered radiation at extreme ultraviolet, soft x-ray, and x-ray wavelengths.

8.1 CONCEPTS OF SPATIAL AND TEMPORAL COHERENCE

The ability to focus radiation to the smallest possible spot size, to propagate it great distances with minimal divergence, to encode wavefronts, and in general to form interference patterns, requires well-defined phase and amplitude variations of the fields throughout the regions of interest. In general, simple phase distributions approaching those of plane or spherical waves are of greatest interest in those applications. Real laboratory sources, especially at very short wavelengths, generally radiate fields with more complex phase relationships that are well defined over only limited spatial and temporal scales. This brings us to the subject of coherence, its technical definition, and various convenient measures.

Coherence in our daily lives refers to a systematic connection or logical relationship between events, actions, or policies. In physics the word implies similar relationships among the complex field amplitudes used to describe electromagnetic radiation. Mathematically, one utilizes a *mutual coherence function*, Γ, as a measure of the degree to which the electric field at one point in space can be predicted, if known at some other point, as a function of their separation in space and time[1, 2]:

$$\Gamma_{12}(\tau) \equiv \langle E_1(t+\tau)E_2^*(t)\rangle \tag{8.1}$$

where in this scalar form E_1 and E_2 are the electric fields at points 1 and 2, and τ is the time delay. The angular brackets denote an expectation value, or a time average of the indicated product. It is often convenient to introduce a normalized *complex degree of coherence*, γ_{12}, again in scalar form, as

$$\gamma_{12}(\tau) = \frac{\Gamma_{12}(\tau)}{\sqrt{\langle|E_1|^2\rangle}\sqrt{\langle|E_2|^2\rangle}} \tag{8.2}$$

where the normalizing factors in the denominator are clearly related to the local intensities at the respective points, as was discussed in Chapter 2, Section 2.3. Thus, for example, in the case of a uniform plane wave, of very well-defined frequency, if the electric field is known at any given space–time point, it can be predicted everywhere else with certainty. As we quantify this later for real physical systems, we will consider this uniform plane wave as *coherent radiation*, meaning that $|\gamma| = 1$ everywhere. The counterexample would be one in which there were a large number of atoms moving randomly and radiating independently, at various frequencies, so that fields at the two separated points have almost no relationship. In this case the resultant degree of coherence, μ, approaches zero, and the fields are considered *incoherent*.

One could write similar functions to describe amplitude and phase correlations in other physical systems. For a well-behaved water wave, for instance, one would expect the surface amplitude to be predictable over great distances, so that $|\gamma|$ would be near unity, implying a high degree of coherence, over much of the observed field. On the other hand, the introduction of randomly thrown pebbles would create a jumble of uncorrelated disturbances, so that $|\gamma|$

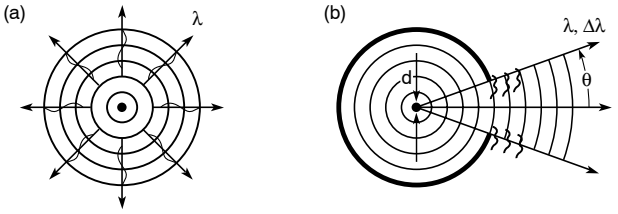

FIGURE 8.1. (a) Fully coherent radiation from a point source oscillator, which oscillates for all time. Note the circular or spherical nature of the outgoing waves. (b) Partially coherent radiation from a source of finite size, emission angle, and duration. Note that the outgoing radiation only approximates circular or spherical waves.

would approach zero in the immediate vicinity, leading us to conclude that the fields in this vicinity were largely incoherent.

To introduce the concept of a *coherence region*, we consider first the rather visual example of soldiers marching across a field. The coherent limit corresponds to all the soldiers in perfect step. In the presence of a strong wind, however, some soldiers might not hear the leader calling the cadence. In this case those soldiers close enough to hear would remain in step, while those further away would become out of step – so there would be a region of coherence near the leader. The distance over which there is a reasonable expectation that the soldiers were marching in step could be called a "coherence length." Note that the coherence length need not be the same in all directions, in this case being dependent on wind direction. The complete absence of cadence would result in uncorrelated stepping, a state of incoherence where $|\gamma|$ goes to zero for the smallest separations, and where the coherence length is essentially zero. In the following paragraphs we will attempt to provide measures of the distances over which electromagnetic fields can be expected to be well correlated, and thus useful for interference experiments as discussed in the first paragraph of this chapter.

In the theoretical limit of a point source oscillating at a single frequency for all time, from minus infinity to plus infinity, the radiated field quantities would be perfectly correlated everywhere. That is, if one knew the electric field amplitude and phase at a given point and time, one would know these quantities at all points and for all time. In this limiting case the radiation field is said to be *coherent*. Real physical sources, however, are made up of spatially distributed radiators that emit with a finite spectral bandwidth for a finite period of time. Consequently, well-defined phase relationships between field amplitudes are in practice restricted to a finite *region of coherence*.

Real sources are neither fully coherent nor fully incoherent, but rather are *partially coherent*.[1] In Figure 8.1(a) the point source radiates fields that are perfectly correlated, and thus coherently related everywhere. In Figure 8.1(b) a source of finite size and spectral bandwidth, restricted to radiate over a limited angular extent, generates fields with strong phase and amplitude correlation over only a limited extent. This brings us again to notions of "regions of coherence" and "coherence time": that is, spatial and temporal measures over which the fields are well correlated. In cases where there is a well-defined direction of propagation, it is convenient to decompose the region of coherence into orthogonal components, one in the direction of propagation and one transverse to it, as illustrated in Figure 8.2. Throughout the remainder of this chapter we will confine ourselves to the subject of partially coherent radiation in which there is a relatively well-defined direction of energy transport.

In the direction of propagation it is common to introduce a longitudinal, or *temporal*, coherence length l_{coh} over which phase relationships are maintained. For a source of bandwidth

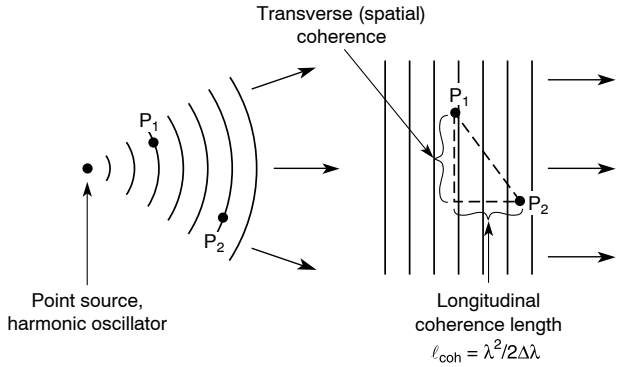

FIGURE 8.2. Transverse and longitudinal coherence.

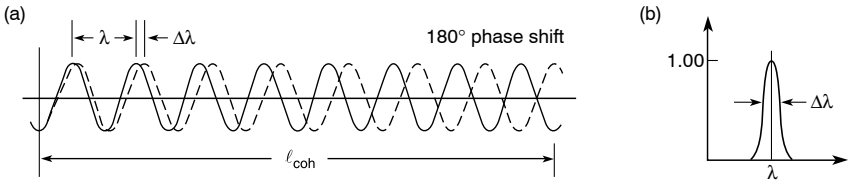

FIGURE 8.3. (a) Spectral bandwidth and (b) coherence length: destructive interference due to finite spectral bandwidth for radiation of wavelength λ and spectral bandwidth $\Delta\lambda$.

$\Delta\lambda$, one can define a coherence length

$$l_{\text{coh}} = \frac{\lambda^2}{2\,\Delta\lambda} \tag{8.3}$$

where $\Delta\lambda$ is the spectral width, as discussed by several authors.[2, 3] The relationship between longitudinal coherence length (e.g., in the direction of propagation) and spectral bandwidth is illustrated in Figure 8.3. Here the coherence length is taken as that distance that results in two waves, of wavelength difference just equal to the bandwidth $\Delta\lambda$, becoming 180° out of phase. Over such a distance one would expect the waves emanating from a source of continuous spectral width to become largely uncorrelated, and thus not contribute significantly to a well-defined interference pattern. Equation (8.3) follows from Figure 8.3 on writing $l_{\text{coh}} = N\lambda$ for the first wave and $l_{\text{coh}} = (N - \frac{1}{2})(\lambda + \Delta\lambda)$ for the spectrally shifted wave, which executes one-half less oscillation (one-half fewer wavelengths) to travel the same distance, and then equating the two to solve for the "number of waves of coherence," $N = \lambda/(2\,\Delta\lambda)$. Equation (8.3) then follows on multiplying N by the wavelength, giving the coherence length for which radiation of continuous bandwidth $\Delta\lambda$ becomes substantially dephased. The resultant numerical factor of $\frac{1}{2}$ appearing in Eq. (8.3) is somewhat arbitrary as obtained here, as it depends on the criteria selected. The numerical factors' dependence on spectral line shape is discussed by Goodman[2] in his Section 5.1.3. In the experimental formation of interference (fringe) patterns by amplitude dissection (e.g., using a beamsplitter) and recombination, as in interferometry[1] and holography,[3] it is essential that differences in propagation length

be less than the coherence length; otherwise high contrast interference patterns will not be obtained.

Transverse, or *spatial*, coherence is related to the finite source size and the characteristic emission (or observation) angle of the radiation. In this case one is interested in phase correlation in planes orthogonal to the direction of propagation. It is instructive to consider the relationship of spatial coherence to spherical waves in the limit of phase being perfectly correlated everywhere. Clearly this limit corresponds to concentric spherical waves with constant phase across every spherical surface and with phase maxima separated by a wavelength in the outward propagation direction. Although somewhat restrictive, we consider the spherical case because it is common to our experience and yields a clear physical insight. Again we consider only a small portion of the spherical wave propagating in a relatively well-defined direction. With some appropriate bandwidth, and thus finite coherence length, such a spherical wave could provide a reference wave for encoding complex wavefronts, as in holography. Near-spherical waves can be focused to a spot size approaching finite wavelength limits, as in a scanning microscope, or collimated to travel with minimal divergence for use in precision diffraction experiments.

Full spatial coherence, the situation in which phase is perfectly correlated at all points transverse to the propagation direction, can be achieved with a spherical wavefront, which we associate with a point source. We might then ask, "How small is a point source?" or more accurately, "How small must the source be to produce wavefronts suitable for our purpose?" and "How small must our undulator electron beam or x-ray laser aperture appear to be in order to provide spatially coherent radiation?" We can obtain a simple estimate based on Heisenberg's uncertainty principle

$$\Delta\mathbf{x} \cdot \Delta\mathbf{p} \geq \hbar/2 \tag{8.4}$$

Here $\Delta\mathbf{x}$ is the uncertainty in position and $\Delta\mathbf{p}$ the uncertainty in momentum, both being single-sided rms ($1/\sqrt{e}$) measures of Gaussian probability distributions.[4] Using Eq. (8.4), we can determine the smallest source size d resolvable with finite wavelength λ and observation half angle θ. For photons the momentum is $\hbar\mathbf{k}$, where the scalar wavenumber $|\mathbf{k}|$ is $2\pi/\lambda$. If the relative spectral bandwidth $\Delta\lambda/\lambda$, which is equal to $\Delta k/k$, is small, then the uncertainty in momentum, $\Delta\mathbf{p} = \hbar\,\Delta\mathbf{k}$, is due largely to the uncertainty in direction θ, so that for small angles $|\Delta\mathbf{p}| = \hbar k\,\Delta\theta$. Substituting into the uncertainty relation (8.4)

$$\Delta x \cdot \hbar k\,\Delta\theta \geq \hbar/2$$

and noting that $k = 2\pi/\lambda$, one has

$$\Delta x \cdot \Delta\theta \geq \lambda/4\pi$$

Identifying the source diameter as $d = 2\,\Delta x$ and the divergence half angle θ with the uncertainty $\Delta\theta$, as illustrated in Figure 8.4, we obtain the limiting relationship[5–7]

$$\boxed{d \cdot \theta = \lambda/2\pi} \tag{8.5}$$

which determines the smallest source size we can discern; that is, within the constraints of physical law we would not be able to tell if our "point" source were any smaller. We recall from Eq. (8.4) that this relationship is for Gaussian rms quantities (d and θ). For non-rms

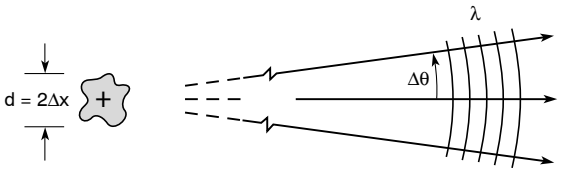

FIGURE 8.4. Spherical wavefronts and spatially coherent radiation are approached when the source size and far-field divergence angle are related to wavelength as indicated in Eq. (8.5).

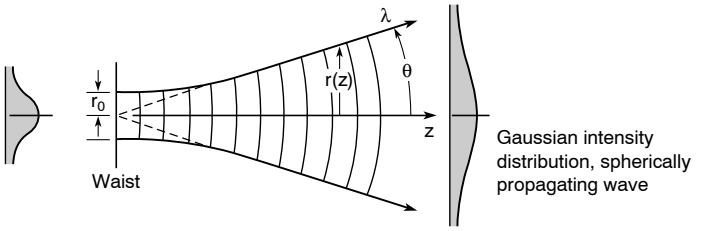

FIGURE 8.5. Propagation of a Gaussian beam.

measures the numerical factor $(1/2\pi)$ will be different.* Radiation satisfying the equality (8.5) is said to be *diffraction limited* – that is, limited by the finite wavelength and observation angle (or numerical aperture θ). To generate a spatially coherent spherical wave we must develop a source – at x-ray wavelengths – that approaches the limiting values set by Eq. (8.5). For symmetry purposes some researchers prefer to introduce a "spatial coherence length," rather than θ. This would clearly depend on distance z from the source; e.g., if one defines $l_{\text{transverse}} \equiv z\theta$, one has

$$l_{\text{transverse}} = \frac{z\lambda}{2\pi d}$$

In this text, we will confine ourselves to the use of the space–angle relationship given in Eq. (8.5).

For comparison, a laser radiating in a single transverse mode TEM_{00} satisfies this same condition when the waist diameter d and far-field divergence half angle θ are written in terms of rms quantities, as illustrated in Figure 8.5. For a spherical wave propagating with a Gaussian intensity distribution, $I/I_0 = \exp(-r^2/2r_0)$, where r_0 is the $1/\sqrt{e}$ waist radius at the origin $(z = 0)$, the intensity distribution grows with a $1/\sqrt{e}$ radius given by[5, 6]

$$r(z) = r_0\sqrt{1 + \left(\frac{\lambda z}{4\pi r_0^2}\right)^2}$$

Thus in the far field, where $z \gg 4\pi r_0^2/\lambda$, the $1/\sqrt{e}$ divergence half angle is

$$\theta \equiv \frac{r(z)}{z} = \frac{\lambda}{4\pi r_0}$$

*For Gaussian intensity distributions measured in terms of FWHM diameter (d) and FWHM angle (2θ), the equivalent relation is $(d \cdot 2\theta)_{\text{FWHM}} = \frac{2\ln 2}{\pi}\lambda = 0.441\lambda$, or approximately $\lambda/2$.

With a waist diameter $d = 2r_0$, this TEM_{00} laser cavity mode exhibits a waist diameter times far-field divergence half angle (both in terms of $1/\sqrt{e}$ measures) given by

$$d \cdot \theta = \frac{\lambda}{2\pi}$$

as found previously in Eq. (8.5) on the basis of Heisenberg's uncertainty principle.

In summary, we now have two convenient relationships by which to gauge the coherence properties of a radiation field for the purpose of conducting phase sensitive interference experiments, Eqs. (8.3) and (8.5):

$$l_{\text{coh}} = \frac{\lambda^2}{2\,\Delta\lambda} \qquad \text{(temporal or longitudinal coherence)}$$

and

$$d \cdot \theta = \lambda/2\pi \qquad \text{(spatial or transverse coherence)}$$

In the next section we will use these measures to determine what fraction of radiated power, or photon flux, from a given source is useful for experiments requiring spatially or temporally coherent radiation within required bounds.

8.2 EXAMPLES OF EXPERIMENTS THAT REQUIRE COHERENCE

As discussed in the preceding section, radiation from a real physical source cannot be truly coherent, because of both the finite spectral width and the finite physical extent. Nonetheless, in many experiments we require a high degree of coherence across only a limited region, and as a consequence may wish to employ spatial and temporal filtering techniques. For example, if one wishes to focus radiation to the smallest possible spot size, at a given wavelength (λ) and lens numerical aperture, the lens must be coherently illuminated, as illustrated in Figure 8.6.

Such focusing is essential for the achievement of highest spatial resolution in a scanning x-ray microscope, a topic we take up in Chapter 9. The advantage of scanning x-ray microscopy is that it is capable of achieving significantly smaller focal spots than are achievable with visible or ultraviolet radiation, and thus it is becoming a widely used tool for the study of material surfaces, chemical fibers, and biological materials. For the case of the smallest possible focal spot size, the lens forms a wavelength-limited image of the source. This process is referred to as *diffraction limited* focusing because the intensity distribution in the focal region is limited by the finite wavelength and lens numerical aperture, rather than the actual source size. This is, of course, a limiting case. For a larger source size the image would simply be demagnified by the ratio $M = q/p$, where q is the source to lens distance, p is the lens to image distance, and these are related to the lens focal length f by the reciprocal thin lens equation $1/f = 1/p + 1/q$. In the diffraction limited case, however, the source size d is sufficiently small that the radiation intercepted by the lens (see θ in Figure 8.6) approximately satisfies the spatial coherence condition set by Eq. (8.5), or its equivalent. In this case the focal

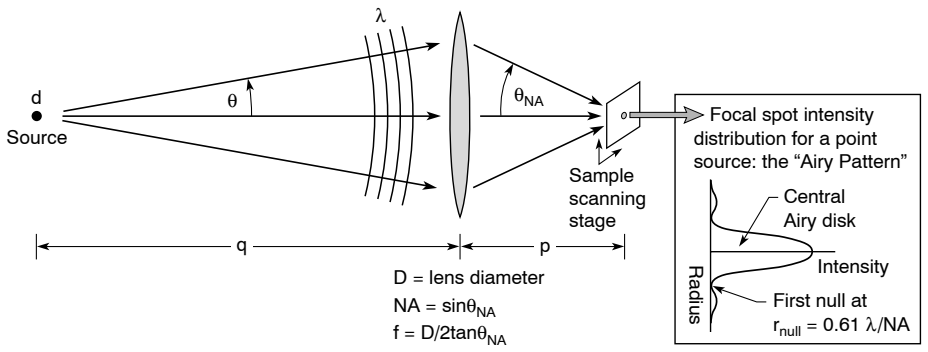

FIGURE 8.6. Diffraction limited focusing – that is, limited only by the finite wavelength and lens numerical aperture (NA) – requires a perfect lens and coherent illumination. The refractive lens shown is for illustration only. At x-ray wavelengths this would require diffractive or reflective optics, such as a Fresnel zone plate or a multilayer coated spherical mirror. In a scanning microscope a sample would be placed at the focus and raster scanned with a suitable translation stage while observing an appropriate signal such as transmitted x-rays, fluorescent emission of characteristic radiation, or photoelectrons. The spatial resolution of the measurement would be set by the focal spot size, assuming this is not compromised by lens imperfections, mounting-related aberrations, improper illumination, or scanning stage limitations such as placement accuracy or non-uniform dwell times.

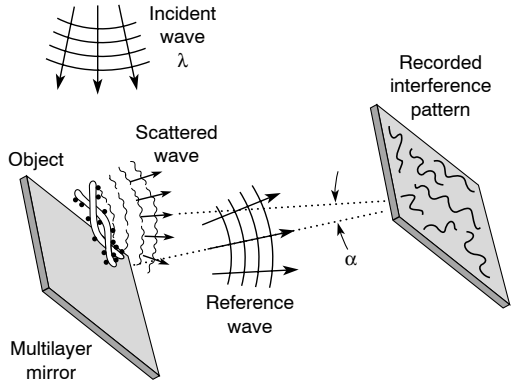

FIGURE 8.7. A possible approach to off-axis x-ray holography, which would require spatially and temporally coherent radiation to achieve high contrast interference patterns.

region intensity pattern approximate an Airy pattern,[1,8] with a focal region radius to the first null given by $0.61\lambda/\mathrm{NA}$. The fact that this is a spherical wave illumination, rather than a plane wave illumination, simply moves the focal plane to a conjugate point determined by the thin lens equation for finite source distance q. Departures from spatially coherent illumination of the lens, due to finite source size and divergence, are addressed in Section 8.6.

A second example in which coherence plays an important role is that of encoding complex wavefronts, as in holography.[3] A typical setup, such as might be used with a weak x-ray scattering object, is shown in Figure 8.7. The incident wave is shown illuminating a flat mirror and a nearby object. After reflection from the multilayer mirror, the radiation propagates

toward the recording medium, and is referred to now as the *reference wave*. In the presence of a weakly scattering object, secondary radiation is scattered in all directions, although Figure 8.7 shows only that portion directed toward the recording plane.

To form an interference pattern in the plane of the recording medium, the reference and scattered waves must maintain a time averaged phase relation, that is, the detected fields must at every point in this plane have a complex degree of coherence [Eq. (8.2)] of order unity, or some fraction thereof, in order to form a recordable interference pattern. Because a complex object, such as the double stranded structure in Figure 8.7, redirects radiation at various angles, leading to a complex jumble of interacting waves at the detector, it is essential that the incident and reference wavefronts maintain a simple variation across the field, such as with the spherical wavefront invoked for development of the spatial coherence condition [Eq. (8.5)], so as to provide a clear mechanism for wavefront encoding and subsequent decoding, or reconstruction, with a similar spherical wavefront. Furthermore, to ensure high contrast encoding (interference) it is essential that all path lengths from the source (not shown) to the detector be equal to within a longitudinal coherence length [Eq. (8.3)], $l_{coh} = \lambda^2/(2\,\Delta\lambda)$, whether that path involves a reflection from the mirror or scattering from the object. The latter condition must be satisfied at every point in the detector plane. Having satisfied these conditions, and with sufficient coherent photon flux or power, a suitable interference pattern can be produced and recorded with an appropriate detector.

In general, the interference pattern at x-ray wavelengths will be characterized by a very fine spatial scale, of order $\lambda/\sin\alpha$, where α is the angle between reference and scattered waves. The geometry of Figure 8.7 is designed to keep these two waves nearly collinear (small α), but sufficiently separated to permit an unambiguous reconstruction – an attribute of off-axis holography. Note that the selected geometry imposes a condition whereby the angle of recorded scattering, which is due to spatial features of the sample, is about equal to the change in direction of the reference wave, which is due to the spatial periodicity of the multilayer mirror. Thus by this technique one would expect, if successful, to image features in the sample with a scale size about equal to a multilayer period. By the Bragg condition discussed in Chapter 4, this is equal to $\lambda/\sqrt{2}$ for a total turning angle of 90°.

This example, however, is presented here to illustrate ideas and concepts rather than to suggest its practical implementation. Although in principle it achieves a resolution equal to the wavelength, large angle x-ray scattering from a non-periodic structure can be expected to be weak. Success for such an experiment would require a high resolution ($\lambda/\sin\alpha$) detector with high (quantum) sensitivity, good dynamic range and linearity, and a radiation source capable of generating radiation with the requisite spatial and temporal coherence at sufficiently high coherent photon flux or coherent power. In the following section we discuss the procedures by which a partially coherent radiation field can be spatially and temporally filtered to achieve the desired degree of coherence. Early examples that demonstrate off-axis holography with a spatially and temporally filtered x-rays are presented in the literature by Aoki, Kikuta, Kohra, and their colleagues.[9] Gabor holography is discussed by Howells, Jacobsen, Kirz, and their colleagues,[10] and soft x-ray interferometry is discussed by Joyeaux and Pollack.[11]

A clever approach to atomic resolution holographic imaging of surface structures is based on the scattering and interference of fluorescence emission. Known as *inside source holography*, the technique does not require coherent illumination, but rather utilizes the inherent coherence of single atom emissions scattered off near neighbors. The resultant interference patterns are summed in the far field over the contributions of many atoms in an identical geometric lattice. First proposed for this application by Szöke, recent experiments are described by Fiagel, Tegze, Marchesini, and their colleagues in reference 9–101.

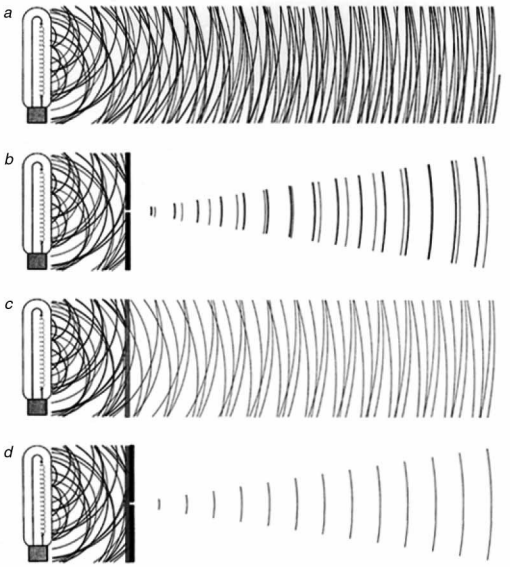

FIGURE 8.8 (see Colorplate IX). Spatial and spectral filtering is illustrated as a procedure to produce coherent radiation, albeit at greatly diminished power, from an ordinary thermal source of visible light. In the nomenclature used here, d would be the diameter of the pinhole shown in part (d), and θ would be the divergence half angle in part (d), set either by the radiation emission characteristics, by a downstream acceptance aperture, or by a lens. (From A. Schawlow,[12] Stanford University.)

8.3 SPATIAL AND SPECTRAL FILTERING

We concluded in Section 8.1 that the limiting condition of spatially coherent radiation is a space–angle product [Eq. (8.5)], or phase space[†] volume

$$d \cdot \theta = \lambda/2\pi$$

where d is a Gaussian $1/\sqrt{e}$ diameter and θ is the Gaussian half angle. All physical sources generate radiation of space–angle product larger than this, often considerably larger. At visible wavelengths, for instance, only lasers with intra-cavity mode control approach this limit, those operating in the so-called TEM_{00} mode.[5] The question here is: what if your source generates radiation into a larger phase space, largely incoherent in nature, but you wish to use it for phase sensitive experiments that require a higher degree of coherence? Schawlow,[12] in his article on lasers, introduces a very informative illustration to show how such radiation can be filtered, both spectrally and spatially, to obtain radiation of greatly improved coherence properties, albeit at the loss of considerable power.

The illustration is reproduced in part here in Figure 8.8. Shown is a typical thermal light bulb with an extended filament heated to a temperature such that many excited atoms randomly

[†]This space–angle product is often referred to as a "phase space" volume. This derives from the study of dynamics, where particles are followed in a position–momentum phase space ($\Delta\mathbf{x}$, $\Delta\mathbf{p}$). For photons $p = \hbar\mathbf{k}$, and for nearly monochromatic radiation the interval in momentum $\Delta\mathbf{p} = \hbar\,\Delta\mathbf{k}$ becomes $\Delta\mathbf{p} = \hbar k\,\Delta\boldsymbol{\theta}$, where $\Delta\boldsymbol{\theta}$ is transverse to $\mathbf{k}$. Thus for nearly monochromatic photons the interval of position–momentum phase space becomes $\Delta\mathbf{x} \cdot \Delta\boldsymbol{\theta}$, which has a scalar minimum given by Eq. (8.5).

radiate a broad spectrum of white light – that is, radiate a continuum containing all colors of the spectrum visible to the human eye. The radiation is filtered in two ways. A pinhole is used [Figure 8.8(b)] to obtain spatially coherent radiation (over some angular extent), as set here by Eq. (8.5). A color filter is used [Figure 8.8(c)] to narrow the spectral bandwidth, thus providing a degree of longitudinal coherence, as described here in Eq. (8.3). Combining both the pinhole and the filter, one obtains radiation that is both spatially and temporally coherent, as is seen in Figure 8.8(d), but with a power that is only a small fraction of the total power radiated by the light bulb.

As Schawlow points out in his article, a visible light laser has the great advantage of providing these desired coherence properties, often with very long temporal coherence length (very narrow $\Delta\lambda/\lambda$), without compromising available power. As we have seen, however, this is a much greater challenge at x-ray wavelengths, both because the energetics make lasing at high photon energy more difficult, and because the very short wavelengths place great demands on the achievement of substantial spatial coherence [Eq. (8.5)]. As a consequence, lasing to date has been accomplished largely at the longer wavelengths of extreme ultraviolet (EUV) and soft x-rays, and has lacked spatial coherence. The techniques of spatial and spectral filtering are therefore very important, and are now commonly used at EUV through x-ray wavelengths. In the following section we discuss the use of spatial and temporal filtering of undulator radiation at powers sufficient to permit experimentation at these very short wavelengths.

8.4 SPATIAL AND SPECTRAL FILTERING OF UNDULATOR RADIATION

As an example of pinhole spatial filtering, Figure 8.9 illustrates how the technique is used to obtain spatially coherent radiation from a periodic undulator,[7, 13] as was described in Chapter 5. The secret to success in this spatial filtering process is that the electron beam cross-section and divergence must be sufficiently small, so that a fair fraction of the radiated flux is able to pass through a pinhole–aperture combination for which $d \cdot \theta = \lambda/2\pi$, as described earlier in Eq. (8.5). That is, viewed through an appropriate pinhole and angular aperture, the radiation must appear to come from a point source. Figure 8.9(a) depicts both the undulator and one form of a spatial filter. Within the indicated central radiation cone (θ_{cen}), the emitted radiation is characterized by a relative spectral bandwidth $\lambda/\Delta\lambda$ equal to N, which is the number of magnet periods and thus the number of oscillations executed by the electrons as they traverse the magnet structure. Figure 8.9(b) shows the calculated power radiated within the central cone [Chapter 5, Eq. (5.41)] for an undulator at the Advanced Light Source (E = 1.9 GeV), which was described previously in Chapter 5, with parameters summarized in Chapter 5, Table 5.1.

In general the phase space of the central radiation cone is larger than the limiting condition [Eq. (8.5)] required for spatial coherence. That is, if we take a typical electron beam diameter of 100 μm and a typical central cone half angle of 50 μrad, the product $d \cdot \theta$ is 5 nm, generally much greater than $\lambda/2\pi$ for EUV and soft x-ray wavelengths. Thus for experiments that require spatial coherence, a pinhole and angular acceptance aperture are introduced, as shown in Figure 8.9(a). This *pinhole spatial filter* is used to narrow, or filter, the phase–space of transmitted radiation, much as was illustrated in Figure 8.8. Filtering to $d \cdot \theta = \lambda/2\pi$ requires the use of both a small pinhole (d) as shown, and some limitation on θ, such that the product is equal to $\lambda/2\pi$. For example, one could accept the full central cone (θ_{cen}) and choose an appropriate pinhole diameter $d = \lambda/2\pi\theta_{\text{cen}}$. Alternatively, one could use a downstream angular aperture (perhaps another pinhole or a lens) of acceptance angle $\theta < \theta_{\text{cen}}$, and choose d accordingly. Both forms of spatial filter are used in practice.

To calculate the spatially coherent power transmitted by the pinhole spatial filter, one must consider the phase–space of the emitted radiation in both the vertical (y–z) and horizontal

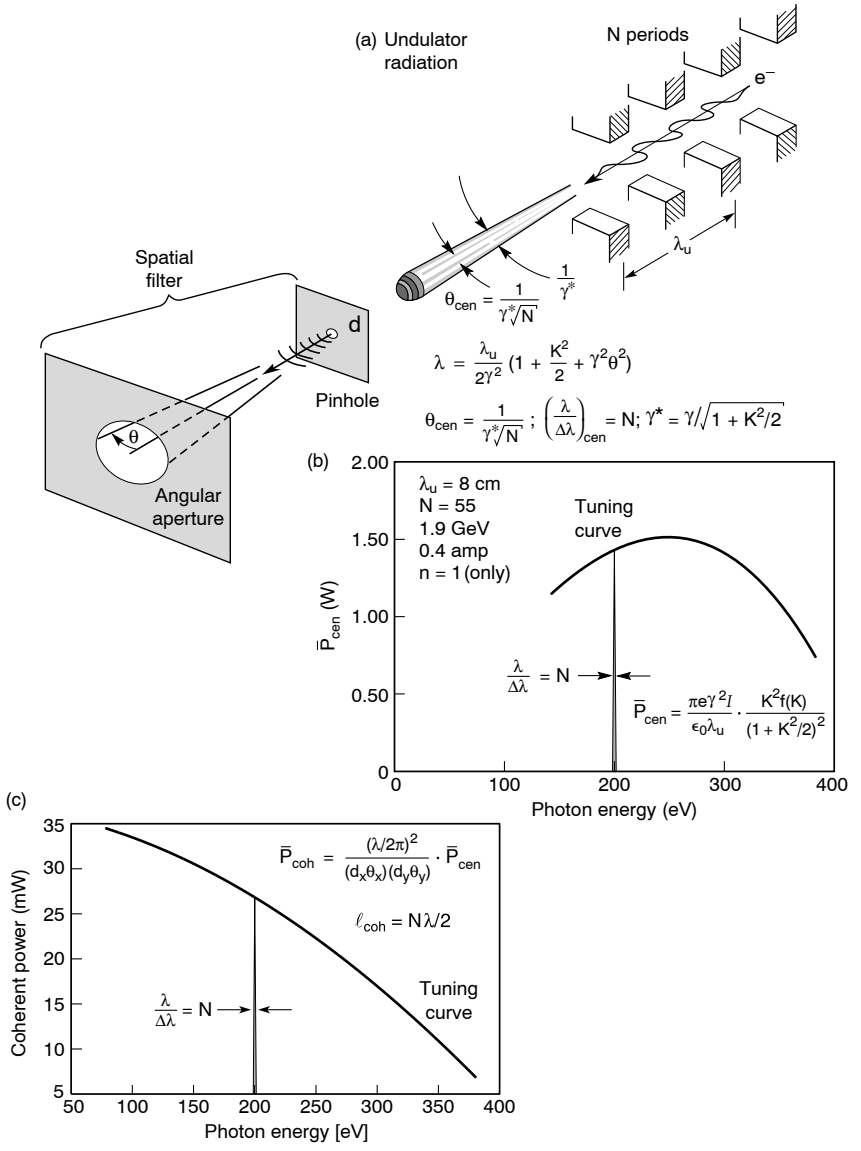

FIGURE 8.9 (see Colorplate X). (a) Undulator radiation with a pinhole spatial filter. (b) Power in the central radiation cone (θ_{cen}, $1/N$ relative spectral bandwidth) for an 8 cm period undulator at the ALS (Table 5.1). (c) Time-averaged coherent power after spatial filtering ($d \cdot \theta = \lambda/2\pi$).

(x–z) planes, as the condition $d \cdot \theta = \lambda/2\pi$ must be satisfied for both. If the electron beam is elliptical, as was discussed in Chapter 5, Section 5.4.5, and illustrated in Figure 5.22, with major and minor diameters $d_x = 2\sigma_x$ and $d_y = 2\sigma_y$, and if the central radiation cone is also somewhat elliptical due to differences in the horizontal and vertical electron beam divergence, so that the characteristic half angles[‡] are θ_x and θ_y, then the respective phase–space volume

[‡]In Eqs. (5.56) these were described as the "total" central cone half angles $\theta_{Tx} = \sqrt{\theta_{\text{cen}}^2 + \sigma_x'^2}$ and $\theta_{Ty} = \sqrt{\theta_{\text{cen}}^2 + \sigma_y'^2}$, where σ_x' and σ_y' are the respective measures of electron beam divergence in the two planes. For simplicity in this chapter we have replaced θ_{Tx} by θ_x and θ_{Ty} by θ_y.

containing the emitted power in the radiation cone, $\bar{P}_{\text{cen}}$ of Eq. (5.41), will be $(d_x\theta_x)(d_y\theta_y)$. The pinhole spatial filter must reduce both $d_x\theta_x$ and $d_y\theta_y$ to $\lambda/2\pi$. The transmitted *spatially coherent power*[7] will therefore be reduced, proportionally, to a value

$$\boxed{\bar{P}_{\text{coh},N} = \left(\frac{\lambda/2\pi}{d_x\theta_x}\right)\left(\frac{\lambda/2\pi}{d_y\theta_y}\right)\bar{P}_{\text{cen}}} \tag{8.6}$$

where the horizontal (x) and vertical (y) phase–space filter factors are written separately to remind us that each alone has a maximum value of unity. In much of what follows we will assume that in both planes $d \cdot \theta > \lambda/2\pi$, permitting some simplifications to the formulae.¶

We recall from Chapter 5, Eq. (5.41a), that

$$\bar{P}_{\text{cen}} = \frac{\pi e\gamma^2 I}{\epsilon_0 \lambda_u} \cdot \frac{K^2}{(1 + K^2/2)^2} f(K)$$

where I is the average current, λ_u is the undulator period, and $f(K)$ is a finite-K correction factor of order unity which is given in Chapter 5, Eq. (5.41). The longitudinal coherence length is understood to be $l_{\text{coh}} = \lambda^2/(2\,\Delta\lambda) = N\lambda$ for N undulator periods and no further spectral filtering. This is consistent with our formulations of $\bar{P}_{\text{cen}}$ and θ_{cen}, which are defined for a relative spectral bandwidth of $\lambda/\Delta\lambda = N$. According to Eq. (8.6), the spatially coherent power can generally be expected to decline with a λ^2 behavior for shorter wavelengths. This phase–space scaling, however, is modified for undulator radiation by several factors that arise from the K-dependence of radiated power, involving the electrons' transverse acceleration, reduced axial velocity, and electron beam divergence parameters.

To examine the wavelength dependence of coherent power further we note that $\bar{P}_{\text{cen}}$ contains a factor $K^2/(1+K^2/2)^2$ that is related to wavelength through the undulator equation [Eq. (5.28)]

$$\lambda = \frac{\lambda_u}{2\gamma^2}\left(1 + \frac{K^2}{2} + \gamma^2\theta^2\right)$$

For on-axis radiation ($\theta = 0$) one has

$$\lambda = \frac{\lambda_u}{2\gamma^2}\left(1 + \frac{K^2}{2}\right)$$

or more conveniently, in terms of photon energy ($\hbar\omega = 2\pi\hbar c/\lambda$),

$$\hbar\omega = \frac{\hbar\omega_0}{1 + K^2/2} \tag{8.7a}$$

where

$$\hbar\omega_0 \equiv 4\pi\hbar c\gamma^2/\lambda_u \tag{8.7b}$$

¶The phase–space assumption $d \cdot \theta > \lambda/2\pi$ is generally valid for the undulator radiation, but is near its limit (diffraction limited radiation) in the vertical plane for longer wavelength radiation at third generation facilities.

is the highest photon energy that can be radiated in the fundamental ($n = 1$) by a given undulator, and that corresponds to the limiting case $K = 0$. With some algebraic manipulation one can show that the three wavelength-dependent factors, λ^2 due to the coherent phase–space constraint, K^2 due to the transverse electron acceleration, and $(1+K^2/2)^2$ due to the decreased axial velocity ($\gamma^* = \gamma/\sqrt{1+K^2/2}$) for finite K, combine to give a photon energy dependence $(\hbar\omega_0 - \hbar\omega)/\hbar\omega$, so that the spatially coherent power [Eq. (8.6)] for an undulator wavetrain of N cycles takes the form

$$\bar{P}_{\mathrm{coh},N} = \frac{e\lambda_u I}{8\pi\epsilon_0 d_x d_y \theta_x \theta_y \gamma^2}\left(\frac{\hbar\omega_0}{\hbar\omega} - 1\right) f(\hbar\omega/\hbar\omega_0) \tag{8.7c}$$

where in terms of photon energy the finite-K correction factor [Eq. 5.41(d)] can be rewritten as

$$f(\hbar\omega/\hbar\omega_0) = \frac{7}{16} + \frac{5}{8}\frac{\hbar\omega}{\hbar\omega_0} - \frac{1}{16}\left(\frac{\hbar\omega}{\hbar\omega_0}\right)^2 + \cdots \tag{8.8}$$

Note that for magnetic tuning of the undulator through a range $0 \le K \le 2$, the photon energy is varied by a factor of three, where now in terms of $\hbar\omega/\hbar\omega_0$ the factor $f(1) = 1$, while for instance $f(\frac{1}{3}) = 0.65$. Equation (8.7), however, does not give the full story, as the product $\theta_x\theta_y$ in the denominator may also contain a noticeable photon energy dependence, depending on the relative values of electron beam divergence $\sigma'_{x,y}$ and the central cone half angle, θ_{cen} [see the footnote below Eq. (8.6)]. For the case where the undulator condition $\sigma'^2_{x,y} \ll \theta^2_{\mathrm{cen}}$ is well satisfied, which corresponds to a relatively narrow spectral shape (see Figure 5.23), the product $\theta_x\theta_y$ can be approximated as

$$\theta_x\theta_y \simeq \theta^2_{\mathrm{cen}} = \frac{1+K^2/2}{\gamma^2 N}$$

which by Eq. (8.7a) becomes $\theta_x\theta_y \simeq \hbar\omega_0/\hbar\omega\gamma^2 N$. The spatially coherent power in this important special case then takes the form

$$\bar{P}_{\mathrm{coh},N} = \frac{e\lambda_u I N}{8\pi\epsilon_0 d_x d_y}\left(1 - \frac{\hbar\omega}{\hbar\omega_0}\right) f(\hbar\omega/\hbar\omega_0) \qquad \left(\sigma'^2 \ll \theta^2_{\mathrm{cen}}\right) \tag{8.9}$$

An example of coherent power versus photon energy is given in Figure 8.9(c) for the case of an 8 cm undulator at the ALS, where $\sigma'_x = 23$ μrad, $\sigma'_y = 3.9$ μrad, and for $K = 1$ (286 eV photon energy, 4.34 nm wavelength) the central cone half angle is 44 μrad, so that the undulator condition is well satisfied. The values of d_x and d_y are 520 μm and 32 μm, respectively. The spatially coherent fraction $(\lambda/2\pi)^2/d_x\theta_x d_y\theta_y$, given in Eq. (8.6), is 1.3×10^{-2} for this undulator at a wavelength of 4.34 nm ($K = 1$, $\hbar\omega = 286$ eV). Thus the 1.4 W power in the central cone is reduced by spatial filtering to a value of 18 mW of spatially coherent power. According to Eq. (8.9), the coherent power is a linearly decreasing function of photon energy, going to zero at $\hbar\omega_0 = 428$ eV. Although the curve in Figure 8.9(c) derives from the more general Eq. (8.7), it very closely follows the specialized form given in Eq. (8.9) for this case where $\sigma'_{x,y} \ll \theta_{\mathrm{cen}}$.

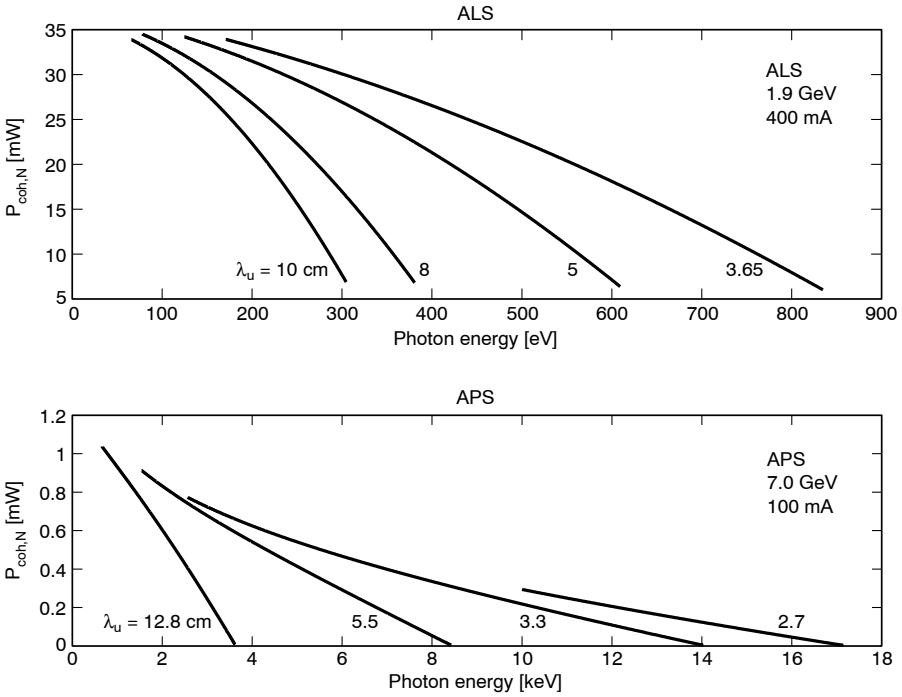

FIGURE 8.10. Spatially coherent average power within a $1/N$ relative spectral bandwidth for undulators at the Advanced Light Source and the Advanced Photon Source, previously described in Chapter 5, with electron beam parameters summarized in Table 5.1. Note that coherent power is shown for the ALS at 1.9 GeV, and for the APS at 7.0 GeV beam energy. Harmonics ($n = 3,\ 5$) can be used to bridge photon energies between those shown. Note that peak powers are nominally 54 times higher than average power values at the ALS, and 100 times higher than average power values at the APS.

Coherent power can be obtained at higher photon energies through the use of shorter undulator periods (λ_u) and higher electron beam energies. This point is illustrated in Figure 8.10, which shows spatially coherent power [Eq. (8.7)] versus photon energy for several undulator periods and differing electron beam energies at the two U.S. synchrotron radiation facilities described in Chapter 5 (Section 5.1 and Table 5.1). These curves are for a longitudinal coherence length $l_{\text{coh}} = N\lambda/2$, where N is the number of periods for each specific undulator. Note that spatially coherent power of order 100 μW is achievable to photon energies as high as 10 keV at the Advanced Photon Source ($E = 7.0$ GeV).

The scaling of coherent power at high photon energy can best be appreciated through examination of Eq. (8.7), where θ_x and θ_y are retained as variables because at high values of γ, θ_{cen} is smaller and possibly comparable to σ_x' and σ_y'. Typical values are given in Table 5.1. With $d_x,\ d_y,\ \theta_x$, and θ_y fixed or slowly varying, and with the factors $(\hbar\omega_0/\hbar\omega - 1)\, f\,(\hbar\omega/\hbar\omega_0)$ providing a local photon energy *shape factor* for a given undulator in the vicinity of its own $\hbar\omega_0$, the wavelength scaling of coherent power is dominated by λ_u/γ^2, which is proportional to λ, or inversely to photon energy, as seen on the more global scale of Figure 8.10. In the vicinity of $\hbar\omega_0$ for any given undulator, λ_u and γ are fixed and the dependence on photon

energy is dominated by the local shape factor described above. The absolute values of coherent power are also affected by the storage ring current I, which is generally less at higher beam energies. Again see Table 5.1 for typical values.

On a more global scale, the coherent power is observed in Figure 8.10 to scale roughly as λ, when corrected for differences in current. From Eq. (8.6) we expect coherent power to scale as λ^2, but higher values of γ are required to reach shorter wavelengths, and the power in the central cone scales as γ^2/λ_u, or as $1/\lambda$, thus giving a net scaling proportional to λ, as seen in Figure 8.10. Note that because of the duty cycle of the synchrotron facilities (e.g., 35 ps FWHM Gaussian pulses every 2.0 ns at the ALS), the peak power can be considerably higher than the average power, for instance, a factor of 54 at the ALS and a factor of 100 at the APS, as discussed in Section 5.4.7.

For many experiments it is also desirable to narrow the spectral bandwidth, either because improved spectral resolution is required to probe atomic or molecular states, because a chromatically sensitive zone plate focusing lens requires a relatively narrow spectral bandwidth (narrower than one divided by the number of zones), or because a longer longitudinal coherence length is required for high contrast interferometric or holographic fringe formation. The radiation must then be spectrally filtered by a monochromator (not shown in Figure 8.9) to further narrow the relative spectral bandwidth to a suitable value of $\Delta\lambda/\lambda$, thus increasing the longitudinal coherence length from a value of $N\lambda/2$ to a greater length $l_{\text{coh}} = \lambda^2/(2\,\Delta\lambda)$. For example, if monochromatization to a value $\lambda/\Delta\lambda = 10^3$ were desired, the longitudinal coherence length would become $l_{\text{coh}} = 10^3\lambda/2$. This of course is accomplished at a reduction in spatially coherent power. By filtering from $\Delta\lambda/\lambda = 1/N$ to $\Delta\lambda/\lambda = 1/10^3$, the transmitted power is necessarily reduced by a multiplicative factor $(\Delta\lambda/\lambda)/(1/N)$, or $N/10^3$ in the example cited. Furthermore, there will be an *insertion loss* due to the finite monochromator efficiency, including such factors as the grating or crystal efficiency, finite mirror reflectivities, etc. If we collect these factors into an inclusive *beamline efficiency* η, then the available coherent power can be written as

$$\bar{P}_{\text{coh},\lambda/\Delta\lambda} = \underbrace{\eta}_{\substack{\text{beamline}\\ \text{efficiency}}} \underbrace{\frac{(\lambda/2\pi)^2}{(d_x\theta_x)(d_y,\theta_y)}}_{\substack{\text{spatial}\\ \text{filtering}}} \cdot \underbrace{N\frac{\Delta\lambda}{\lambda}}_{\substack{\text{spectral}\\ \text{filtering}}} \cdot \bar{P}_{\text{cen}} \tag{8.10a}$$

which can be rewritten following the logic that led to Eq. (8.7) as

$$\bar{P}_{\text{coh},\lambda/\Delta\lambda} = \frac{e\lambda_u I(\eta N\,\Delta\lambda/\lambda)}{8\pi\epsilon_0 d_x d_y \theta_x \theta_y \gamma^2}\left(\frac{\hbar\omega_0}{\hbar\omega} - 1\right) f(\hbar\omega/\hbar\omega_0) \tag{8.10b}$$

where $\lambda/\Delta\lambda$ is the relative spectral bandwidth, N is the number of undulator periods, η is the beamline efficiency (insertion loss), $\hbar\omega_0 = 4\pi c\hbar\gamma^2/\lambda_u$ is the highest photon energy achievable with the fundamental ($n = 1$) of a given undulator in the limit $K = 0$, and $f(\hbar\omega/\hbar\omega_0)$ is the finite-K correction factor for central cone radiation expressed in terms of $\hbar\omega/\hbar\omega_0$ as in Eq. (8.8). To emphasize the penalty paid for this further monochromatization we have bracketed the quantity $\eta N\,\Delta\lambda/\lambda$, which is a numerical factor less than unity that represents the loss of power incurred through monochromatization.

In the case where the undulator condition is well satisfied ($\sigma'_{x,y} \ll \theta_{\text{cen}}$), such that $\theta_x \theta_y \simeq (1 + K^2/2)/N\gamma^2$, the expression for coherent power takes the form

$$\bar{P}_{\text{coh},\lambda/\Delta\lambda} = \frac{e\lambda_u I \eta(\Delta\lambda/\lambda)N^2}{8\pi\epsilon_0 d_x d_y} \cdot \left(1 - \frac{\hbar\omega}{\hbar\omega_0}\right) f(\hbar\omega/\hbar\omega_0) \qquad \left(\sigma'^2 \ll \theta_{\text{cen}}^2\right) \tag{8.10c}$$

which we note scales as N^2 in this limit. This expression is quite accurate for low emittance[§] soft x-ray synchrotron facilities such as the ALS and its equivalent elsewhere, as the condition $\sigma_{x,y}^2 \ll \theta_{\text{cen}}^2$ is reasonably well satisfied for $\gamma \simeq 3728$, $N \simeq 50$–100, and $\sigma' \leq 20$ μrad. Note that while in this case the coherent power scales as N^2, in the case where $\sigma' \simeq \theta_{\text{cen}}$, as may occur for high γ facilities, Eq. (8.10b) must be used and the scaling of coherent power will be closer to linear in N.

In the example cited previously for an 8 cm period undulator at the Advanced Light Source, a monochromator and beamline optics, with an overall efficiency η of 10% (30% grating efficiency and five glancing incidence mirrors at 0.8 reflectivity each) are used to obtain $\lambda/\Delta\lambda = 10^3$. The resultant coherent power at 4.3 nm wavelength (286 eV) would be [following Eq. (8.10a)] $(\frac{1}{10})(0.013)(55/10^3)(1.4\text{ W})$, or about 100 μW, with a longitudinal coherence length of $10^3\lambda = 3.5$ μm. The detailed photon energy (wavelength) dependence is included in Eq. (8.10c).

An example of a beamline designed for spatial and spectral filtering of soft x-ray and extreme ultraviolet (EUV) undulator radiation is shown in Figure 8.11. It employs a grazing incidence grating monochromator[14, 15] as appropriate for use at these wavelengths. (There is extensive recent literature on the design of grating monochromators.[16–18])

The first optical element (M1) is a water cooled plane mirror set at an angle that reflects the desired radiation but absorbs the unwanted power residing in higher harmonics. Following this are curved reflective optics that form an image of the radiating electrons at 65 : 1 spatial demagnification on a downstream entrance pinhole. As with any imaging system, this provides a concomitant increase in angular illumination ($65\theta_{\text{cen}} \simeq 2.9$ mrad at $K = 1$), as required in this case for the downstream experiment, which here involves coherent interferometry of EUV optical systems. With this relatively large angular illumination, pinholes of about 1 μm diameter are required to approximate the condition [Eq. (8.5)] for spatial coherence at 13 nm wavelength.[‖] Also included in the beamline optics is a combined grazing incidence grating and exit slit that provides the desired wavelength and spectral bandpass. Use of a varied line space grating permits wavelength tuning without movement of the (fixed) exit slit.[14, 15] The remaining mirrors permit an intermediate image of the source at the exit slit of the monochromator, with final vertical and horizontal image formation at the pinhole. Though separate branchlines for coherent optics and photoemission microscopy are shown, details of the beamline optics are omitted.

Calculations of the anticipated coherent power available with this undulator and beamline combination are shown in Figure 8.11(b), for a monochromator setting of $\lambda/\Delta\lambda = 10^3$, so that

[§]The phrase "low emittance" refers to an electron beam of small (phase space) product $\pi\sigma\sigma'$. The phrase is occasionally used to describe the facility as well.

[‖]The work at 13 nm wavelength involves the use of Mo–Si multilayer mirrors, as discussed in Chapter 4. The coated optics are used for reduction imaging in the EUV lithography program, as discussed in Chapter 10, Section 10.2.

Chapter 9

SOFT X-RAY MICROSCOPY WITH DIFFRACTIVE OPTICS

Zone Plate Lens

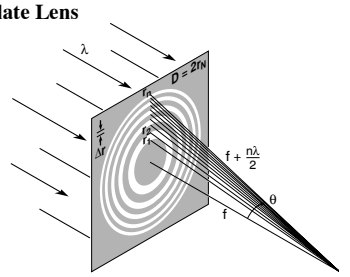

Soft X-Ray Microscope

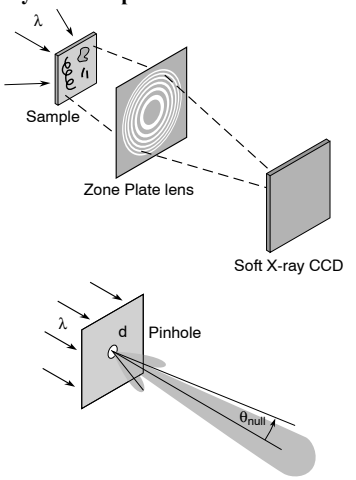

Scanning Soft X-Ray Microscope

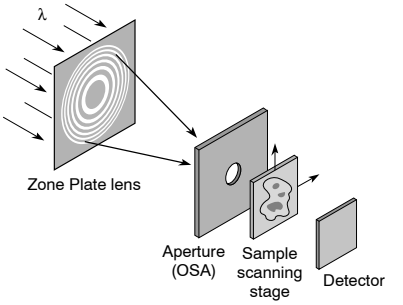

Zone Plate Formulae

$$r_n^2 = n\lambda f + \frac{n^2\lambda^2}{4} \tag{9.9}$$

$$D = 4N\Delta r \tag{9.13}$$

$$f = \frac{4N(\Delta r)^2}{\lambda} \tag{9.14}$$

$$NA = \frac{\lambda}{2\Delta r} \tag{9.15}$$

$$F^{\#} = \Delta r/\lambda \tag{9.16}$$

$$\text{Rayleigh res.} = \frac{0.610\lambda}{\text{NA}} = 1.22\Delta r \tag{9.47, 9.48}$$

$$\text{DOF} = \pm\frac{1}{2}\frac{\lambda}{(\text{NA})^2} = \pm\frac{2(\Delta r)^2}{\lambda} \tag{9.50, 9.51}$$

$$\frac{\Delta\lambda}{\lambda} \leq \frac{1}{N} \tag{9.52}$$

Pinhole Formula

$$\theta_{\text{null}} = 1.22\lambda/d \tag{9.36}$$

In this chapter we consider Fresnel zone plates, particularly as they are used as diffractive image forming lenses for high resolution soft x-ray microscopy. We begin with a relatively simple approach based on our general experience with interference phenomena. From this we obtain a physical appreciation for zone plate performance, and derive most of the useful formulae summarized on this page. We also describe the complementary features of various zone plate microscopes. We next consider formal diffraction theory to better understand the limits of spatial resolution. Pinholes are also considered, as they play an essential role in generating the spatially coherent radiation required for scanning microscopy and other applications involving spatially coherent short wavelength radiation. Finally, we conclude with applications of soft x-ray microscopy to the physical and life sciences, and a short section on the fabrication of zone plates.

9.1 INTRODUCTION

In previous chapters we have discussed the various ways in which radiation can be redirected for image formation, spectroscopic, and other applications. In Chapter 1, Figure 1.13, we summarized the basic processes of scattering, diffraction, refraction, and reflection. In Chapter 3 we studied refraction, the bending of radiation paths at the interface between materials of differing refractive index $n = 1 - \delta + i\beta$. For EUV and soft x-ray wavelengths, we observed that for all materials the ratio β/δ is sufficiently close to unity that significant refraction cannot be obtained within an absorption length. As a consequence the formation of real images by refraction of EUV or soft x-ray radiation is impractical. Glancing incidence total external reflection with curved optics provides a successful path to image formation, particularly at EUV, soft x-ray, and x-ray wavelengths where there are few competing techniques; but the image resolution is significantly compromised by aberrations. Multilayer coatings extend the use of reflective optics, as discussed in Chapter 4, particularly at EUV wavelengths longer than 5 nm, where normal incidence coatings achieve high reflectivity. With high quality curved substrates, multilayer coated mirrors permit near-diffraction-limited imaging in the EUV region, i.e., limited only by the wavelength and numerical aperture of the system.

At shorter wavelengths, particularly in the soft x-ray region extending from perhaps 0.3 nm to 5 nm, diffractive techniques using Fresnel zone plate lenses of various forms are of great interest[1–5] because of their ability to form images at very high spatial resolution, approaching the diffraction limit. Diffraction is the process by which radiation is redirected near sharp edges. As it propagates away from these sharp edges or obstacles, it interferes with nearby undiffracted radiation, producing bright and dark bands known as interference patterns. Because the diffracted radiation propagates in a new direction, the dark and bright interference patterns appear to move laterally with distance away from the obstruction. For small diffracting structures such as disks, pinholes, and gratings (repetitive lines and spaces) it is found that these diffraction patterns, and the energy they represent, propagate away from the structure at angles of order $\theta \sim \lambda/d$, where d is a characteristic dimension. With repetitive structures, such as transmission gratings, consisting of many parallel lines and spaces, the positive interference in certain directions can lead to a very strong redirection of energy. This is also possible in circular geometries, with proper placement of the radial zones, so that positive interference of the diffracted radiation occurs at a well-defined downstream position. This downstream distance is known as the focal length, and the appropriate structure that leads to this focusing of energy is known as a Fresnel zone plate lens. Capable of spatial resolution measured in tens of nanometers, these diffractive lenses are especially valuable for the study of microscopic objects of limited lateral dimensions.

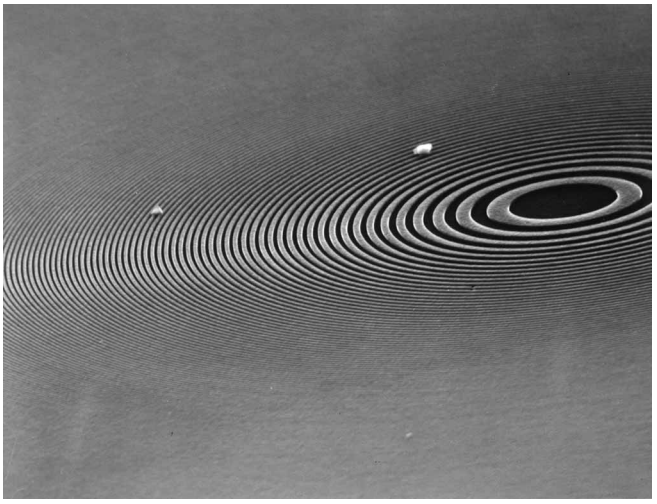

FIGURE 9.1. A Fresnel zone plate lens used for x-ray microscopy. (Courtesy of E. Anderson, LBNL.)

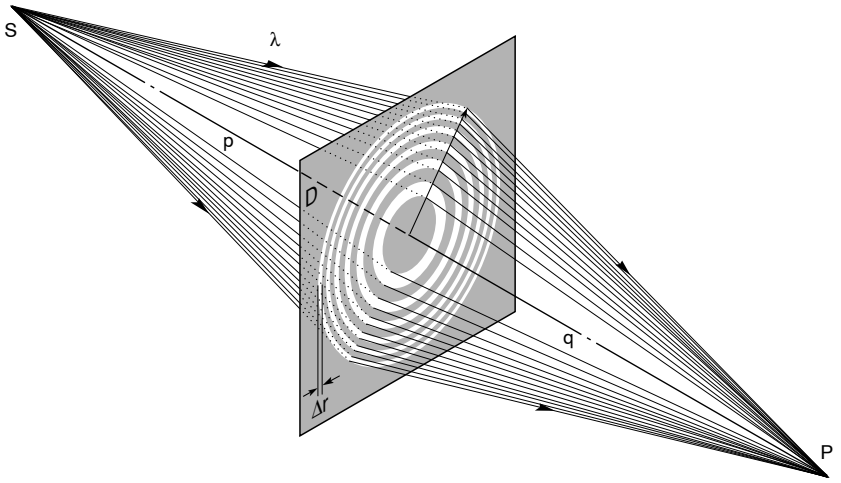

FIGURE 9.2. A Fresnel zone plate used as a diffractive lens to form an x-ray or EUV image of a source point S in the image plane at P. The lens is shown as having a diameter D and outer zone width Δr. The object and image distances are p and q, respectively.

Figure 9.1 shows a zone plate lens used in soft x-ray microscopy. Figure 9.2 illustrates the general technique for point to point imaging with a Fresnel zone plate lens. In its simplest form the zone plate consists of alternating opaque and transparent zones, essentially a circular grating, with radial zones located such that the increased path lengths through sequential transparent zones differ by one wavelength each and thus add in phase at the image point.[6–13] In this manner, on a point by point basis, the image of a full two-dimensional object can be formed in the image plane, using essentially incoherent radiation. As we understand from the previous chapter, the smallest possible spot size that can be formed at P is obtained with

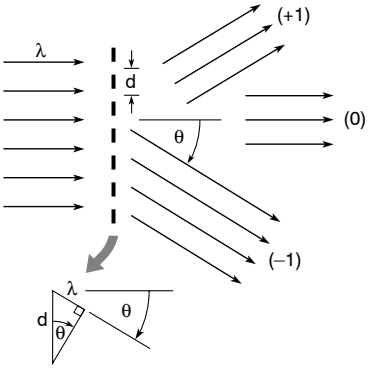

FIGURE 9.3. Diffraction from a transmission grating showing only the 0th and ±1st orders. Higher orders are omitted for clarity. Constructive interference of the diffracted radiation occurs at angles where the path length increases by λ for each additional period d of the grating, such that $\sin\theta = \lambda/d$ in first order.

spatially coherent illumination of the zone plate, a subject of interest for the formation of scanning spot microscopes, which we discuss in the following paragraphs. Of interest here as well is the practical case of partially coherent radiation and the potential advantage this has for image formation and resolution.

We begin our analysis with a simple transmission grating, as illustrated in Figure 9.3. Constructive interference occurs, in first order, at angles where the path length is increased by one wavelength, such that

$$\sin\theta = \frac{\lambda}{d} \tag{9.1}$$

This occurs for both positive and negative angles, giving rise to the ±1st orders of the grating, in addition to the 0th order in the forward direction. Higher orders will be generated at angles θ_m, corresponding to increased path lengths $m\lambda$, such that

$$\boxed{\sin\theta_m = \frac{m\lambda}{d}} \tag{9.2}$$

where $m = 0,\ \pm1,\ \pm2,\ \pm3, \ldots$. For radiation incident on the grating at an angle θ_i, measured from the normal, one readily shows that the condition for constructive interference is

$$\boxed{\sin\theta - \sin\theta_i = \frac{m\lambda}{d}} \tag{9.3}$$

where again $m = 0,\ \pm1,\ \pm2,\ \pm3, \ldots$. Equation (9.3) is known as the *grating equation*, and Eq. (9.2) is clearly a special case of it for normal incidence.

The fraction of incident energy diffracted into the various orders depends on the nature of the periodic structure, i.e., the sharpness of profile, the bar to space ratio (line width as a fraction of grating period), and the complex refractive index, which affects the absorption and phase shift in the grating. For a transmission grating of opaque lines of width equal to half the grating period, as illustrated in Figure 9.4, one can represent the transmission function in

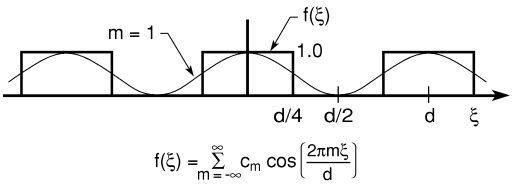

FIGURE 9.4. Representation of a transmission grating of unit absorption in terms of Fourier components. Each component m of the expansion represents an equivalent thin grating, where the coefficient c_m is related to the amount of energy diffracted to a given order m, and where the period d/m is related to the angle of diffraction for that order. Only the first term ($m = 1$) in the expansion is shown. The first coefficients are $c_0 = \frac{1}{2}$, $c_1 = 1/\pi$, $c_2 = 0$, $c_3 = 1/3\pi$, etc., as derived in the text.

a Fourier series expansion, taking even (cosine) terms only for the coordinate choice taken:

$$f(\xi) = \sum_{m=-\infty}^{\infty} c_m \cos\left(\frac{2\pi m\xi}{d}\right) \tag{9.4}$$

with coefficients

$$c_m = \frac{1}{d}\int_{-d/2}^{d/2} f(\xi)e^{-2\pi i m\xi/d}\, d\xi$$

where $f(\xi) = 1$ in the interval $|\xi| \leq d/4$, and $= 0$ in the interval $d/4 < \xi \leq d/2$. Substituting for $f(\xi)$, noting that $e^{-i\theta} = \cos\theta - i\sin\theta$ (Appendix D) and that the sine term does not contribute in this even interval, the integral for the coefficient becomes

$$c_m = \frac{2}{d}\int_0^{d/4} \cos\left(\frac{2\pi m\xi}{d}\right) d\xi$$

$$c_m = \frac{\sin(m\pi/2)}{m\pi} \tag{9.5}$$

By L'Hospital's rule, $c_0 = \frac{1}{2}$. The even order coefficients are all zero, due to the symmetry of the problem with this choice of coordinate origin. The odd order coefficients are $c_m = 1/\pi,\ -1/3\pi,\ 1/5\pi, \ldots$, for $m = \pm 1,\ \pm 3,\ \pm 5, \ldots$, respectively.

We can now represent the single rectangular grating of unit absorption by a superposition of thin cosine gratings of increasing spatial frequency $k_m = 2\pi m/d$ and transmission c_m. Each such grating corresponds to one term in the expansion, leading to radiation of the various diffractive orders m, at angles θ_m described earlier in Eq. (9.2), and associated electric fields $E_m = c_m E_0$, where E_0 is the incident electric field at the grating. From Chapter 3, Eqs. (3.18–3.20), it follows that the intensities of the various diffractive orders are given by

$$I_m = \sqrt{\epsilon_0/\mu_0}|E_m|^2 = |c_m|^2 I_0 \tag{9.6}$$

so that the efficiencies $\eta_m = I_m/I_0$ for diffraction to the various orders are proportional to $|c_m|^2$, and thus from Eq. (9.5)

$$\eta_m = \begin{cases} 0.25 & m = 0 \\ 1/m^2\pi^2 & m \text{ odd} \\ 0 & m \text{ even} \end{cases} \tag{9.7}$$

For an opaque transmission grating of equally wide lines and spaces, 25% of the incident energy is in the 0th order, approximately 10% is diffracted to each of the ±1st orders, and so forth, while the grating itself absorbs 50% of the incident energy.[14, 15]

In phase gratings the opaque lines are replaced by partially transmitting materials to reduce absorptive losses. For materials and wavelengths for which β/δ is minimal, and for thicknesses that permit a relative propagation phase shift approaching π, this can lead to a significant enhancement of diffraction efficiency.

The coefficients in Eq. (9.7) correspond to a symmetric grating of equal line and space widths, permitting a representation [Eq. (9.4)] involving only even cosine functions. For an asymmetric grating involving unequal line and space widths, odd sine functions would also be required. An example would be a grating with line widths equal to $\frac{1}{3}$ the grating period and open spaces of width equal to $\frac{2}{3}$ of the grating period. In such cases the asymmetry (sine terms) leads to non-zero even orders, i.e., finite values of $|c_m|^2$ for $m = \pm 2,\ \pm 4$, etc. This is very much analogous to the discussion of even multilayer diffraction orders for asymmetric coatings of $\Gamma \neq 0.5$, as discussed in Chapter 4, Section 4.2 and Figure 4.4 therein. This subject is relevant here, as we shall shortly consider the diffraction efficiency of zone plate lenses.

For symmetric structures of equal area in successive zones (opaque and transmissive) we will again find only odd orders, $m = \pm 1$, etc. The even orders ($m = \pm 2$) will cancel at the focal point. However, for asymmetric zones of unequal successive areas, even orders do appear. An example of this would be a zone plate where the alternate open zones are narrower than prescribed due to imperfections in the fabrication process. Depending on the degree of asymmetry, even orders of various intensities would appear.

An extensive literature exists on the subject of diffraction from transmission and reflection gratings. In particular see Born and Wolf[14] for an extensive introduction, Hecht[13] for a tutorial on blazed reflection gratings, Morrison[15] for a description of phase gratings at short wavelengths, and Michette[12] for a general description of diffraction gratings at soft x-ray wavelengths. Variable line space gratings are discussed by Hettrick and Underwood and their colleagues.[16–17] The topic of EUV/soft x-ray gratings continues to be one of active research, with applications in many fields, including synchrotron radiation, astrophysics, plasma physics, and fusion. Several recent books specifically addressing this spectral region add to the wealth of valuable literature on the subject of reflection and transmission gratings.[18–20]

In the next section we discuss Fresnel zone plates as circular diffraction gratings that also generate many orders, some of which are diffracted radially inward toward the optic axis and can form a real image (the positive orders), and some of which are diffracted radially outward, forming a virtual image (the negative orders).

9.2 THE FRESNEL ZONE PLATE LENS

The focusing properties of a Fresnel zone plate lens can be understood by considering the first order diffraction from a circular grating with the zonal periods adjusted so that at increasing radius from the optic axis the periods become shorter, and thus by Eq. (9.1) the diffraction angle becomes larger, thus permitting a real first order focus, as illustrated in Figure 9.5. If one draws a right triangle with the focal length f as one side, the radius of any zone r_n as a second side, and the hypotenuse of length $f + n\lambda/2$, then by the Pythagorean theorem the zonal radii are given by

$$f^2 + r_n^2 = \left(f + \frac{n\lambda}{2}\right)^2 \tag{9.8}$$

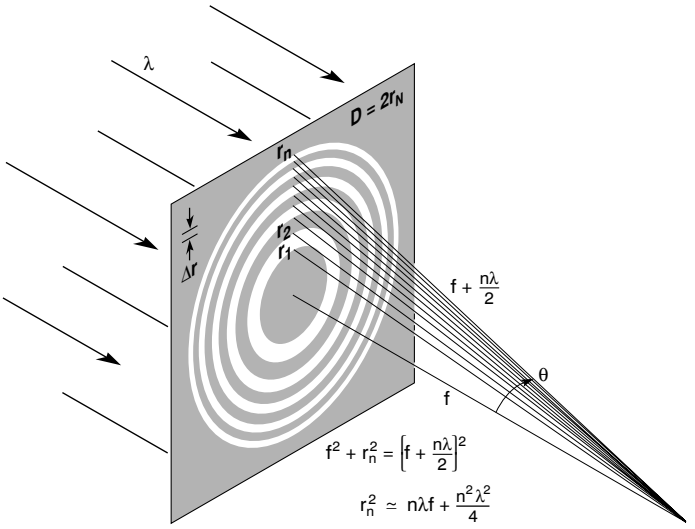

FIGURE 9.5. A Fresnel zone plate lens with plane wave illumination, showing only the convergent (+1st) order of diffraction. Sequential zones of radius r_n are specified such that the incremental path length to the focal point is $n\lambda/2$. Alternate zones are opaque in the simple transmission zone plate. With a total number of zones N the zone plate lens is fully specified. Lens characteristics such as the focal length (f), diameter (D), and numerical aperture (NA) are described in the text in terms of λ, N, and Δr, the outer zone width.

which upon expansion and consolidation of like terms becomes

$$r_n^2 = n\lambda f + \frac{n^2\lambda^2}{4} \tag{9.9}$$

The term $n^2\lambda^2/4$, which represents spherical aberration, can be ignored for $f \gg n\lambda/2$, which we will see shortly corresponds to a lens of small numerical aperture $\mathrm{NA} = \sin\theta = \lambda/(2\,\Delta r) \ll 1$, as is often the case at x-ray wavelengths. Where this is not the case, perhaps with a larger NA optic at an EUV wavelength, the term should be retained. For the low NA case Eq. (9.9) simplifies to

$$r_n \simeq \sqrt{n\lambda f} \tag{9.10}$$

showing that a real first order focus is achieved when successive zones increase in radius by $\sqrt{n}$, providing the desired prescription by which the radial grating period must decrease in order to provide a common focus. The earliest known record regarding the demonstration of focusing light with alternately opaque Fresnel zones is that of Lord Rayleigh in 1871.[6]

We can now obtain expressions for the lens diameter D, focal length f, numerical aperture $\mathrm{NA} = \sin\theta$, spatial resolution, and depth of focus. We choose to do this in terms of the wavelength λ, the total number N of zones, and the outer zone width Δr. We do this from an experimental point of view. In designing an experiment the wavelength is often a first priority, driven by the elemental composition of the material or sample under study and their characteristic absorption and emission lines. In microscopy the next priority is the spatial

resolution required to see features of interest. For zone plate lenses the spatial resolution limit is set by the outer zone width Δr, as we will see shortly. As our third choice we take N, the total number of zones. As we will see in the following paragraphs, zone plate lenses are highly chromatic, that is, the focal length of the lens varies strongly with wavelength. Thus for precise imaging it is necessary to restrict the illumination spectral bandwidth, $\Delta\lambda/\lambda$. We will see shortly that there is an inverse relationship between $\Delta\lambda/\lambda$ and N, the total number of zones. Thus the total number of zones N will be restricted by the relative spectral bandwidth. With this motivation we proceed in the following paragraphs to develop relationships for f, D, NA, resolution, and depth of focus in terms of λ, Δr, and N.

We begin by defining the outer zone width for $n \to N$,

$$\Delta r \equiv r_N - r_{N-1} \tag{9.11}$$

where N is the total number of zones, i.e., the sum of both opaque and transparent zones (twice the number of radial periods). The outer zone width Δr provides a very convenient parameter, and is useful in expressions for other lens parameters.

Now we write Eq. (9.10) twice, once for r_N and once for r_{N-1}, and subtract as follows:*

$$r_N^2 - r_{N-1}^2 = N\lambda f - (N-1)\lambda f = \lambda f$$

Using the definition of Δr given in Eq. (9.11), one also has for the left side of the above equation

$$r_N^2 - (r_N - \Delta r)^2 = 2r_N\,\Delta r - (\Delta r)^2 \simeq 2r_N\,\Delta r$$

since $\Delta r \ll r_N$ for large N. Combining the above two equations, one obtains

$$2r_N\,\Delta r \simeq \lambda f$$

or

$$D\,\Delta r \simeq \lambda f \tag{9.12}$$

From Eq. (9.10) we note that $\lambda f \simeq r_N^2/N$, so that from Eq. (9.12) one has

$$D\,\Delta r \simeq \frac{r_N^2}{N} = \frac{D^2}{4N}$$

or

$$\boxed{D \simeq 4N\,\Delta r} \tag{9.13}$$

The focal length can then be obtained from Eq. (9.12) as

$$f \simeq \frac{D\,\Delta r}{\lambda}$$

*Note that the area of successive zones, $\pi(r_n^2 - r_{n-1}^2) = \pi\lambda f$, is a constant, at least within the long focal length, small NA approximation leading from Eq. (9.9) to Eq. (9.10). Thus the areas of all zones are equal and contribute equally to the intensity of focus.

or in combination with Eq. (9.13)

$$\boxed{f \simeq \frac{4N(\Delta r)^2}{\lambda}} \tag{9.14}$$

This is a very important relationship for the design of zone plate microscope lenses in that it shows that the focal length scales directly with the number of zones, with the square of the outer zone width (which essentially sets the resolution), and inversely with the wavelength, thus introducing a strong chromatic effect.

The numerical aperture (NA) of a lens is defined as

$$\text{NA} \equiv \sin\theta$$

where θ is the half angle measured from the optic axis at focus back to the lens, as illustrated here in Figure 9.5. Thus the numerical aperture of a zone plate lens is given by $\text{NA} = r_N/f = D/2f$, or from Eq. (9.12)

$$\boxed{\text{NA} \simeq \frac{\lambda}{2\,\Delta r}} \tag{9.15}$$

which is a particularly simple form that will be convenient when considering spatial resolution. A related quantity is the lens *F-number*, which we will abbreviate as $\text{F}^{\#}$, defined as

$$\text{F}^{\#} \equiv \frac{f}{D}$$

or again using Eq. (9.12)

$$\text{F}^{\#} \simeq \frac{\Delta r}{\lambda} \tag{9.16}$$

We will return to these parameters in the following section on spatial resolution, depth of focus, and chromatic aberration.

In the preceding paragraphs we have considered the focusing conditions for a zone plate lens with plane wave illumination, as illustrated in Figure 9.5. Next we consider the point by point imaging of an object at a finite distance q from the zone plate, to an image plane at a distance p, as illustrated in Figure 9.6.

Again the successive zones, alternately transmissive and opaque, are constructed so as to add $\lambda/2$ to successive path lengths, so that

$$q_n + p_n = q + p + \frac{n\lambda}{2}$$

where for modest numerical aperture lenses

$$q_n = \left(q^2 + r_n^2\right)^{1/2} \simeq q + \frac{r_n^2}{2q}$$

$$p_n = \left(p^2 + r_n^2\right)^{1/2} \simeq p + \frac{r_n^2}{2p}$$

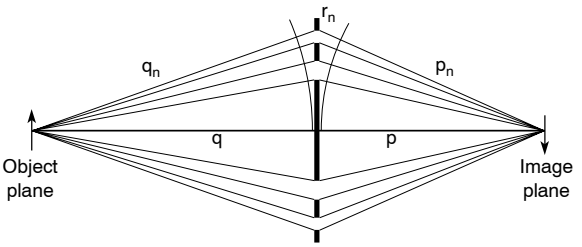

FIGURE 9.6. Point by point imaging with a Fresnel zone plate lens is illustrated. Successive propagation paths are increased by $\lambda/2$.

so that

$$q + \frac{r_n^2}{2q} + p + \frac{r_n^2}{2p} \simeq q + p + \frac{n\lambda}{2}$$

$$\frac{r_n^2}{2q} + \frac{r_n^2}{2p} \simeq \frac{n\lambda}{2}$$

$$\boxed{\frac{1}{q} + \frac{1}{p} \simeq \frac{1}{f}} \tag{9.17}$$

where from Eq. (9.10), $f = r_n^2/n\lambda$. Equation (9.17) relates the image and object distances to the focal length as for an ordinary visible light refractive lens. Similarly, one can show that the transverse magnification is

$$\boxed{M = \frac{p}{q}} \tag{9.18}$$

We now have a basic understanding of how a Fresnel zone plate can be used both to focus radiation and to form a real image of an extended object using first order diffraction.

Recall, however, that a transmission grating generates many orders, thus complicating the use of a zone plate lens and leaving only a fraction of the available photons for the primary purposes of a given experiment. The procedure, suggested in Figure 9.5, of adding a path length of $n\lambda/2$ for constructive interference of sequential zones in first order can be extended to the higher orders ($m = 2,\ 3,\ \ldots$) by adding path lengths $mn\lambda/2$. Following the same procedures used in the preceding paragraphs for the first order ($m = 1$), one finds that the radial zones correspond to phase advances for the higher order diffracted waves given by

$$r_n^2 \simeq mn\lambda f_m \tag{9.19}$$

for zones $n = 0, 1, 2, \ldots$ and diffractive orders $m = 0,\ \pm 1,\ \pm 2, \ldots$, and with corresponding

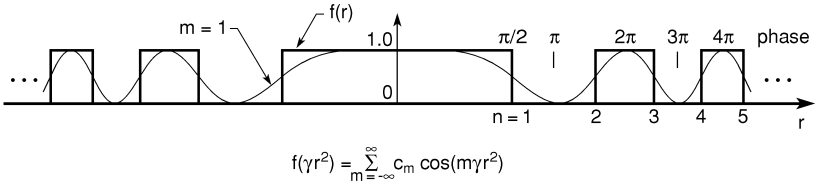

FIGURE 9.7. Representation of a Fresnel zone plate as a transmission grating in terms of the radius squared. Only the first term ($m = 1$) is shown.

focal lengths given by

$$f_m = \frac{f}{m} \tag{9.20}$$

where we note that the negative orders give rise to virtual foci of negative focal length. The diffraction efficiencies of the various orders can be analyzed much like the transmission grating efficiencies of the previous section [see Eqs. (9.4) and (9.5)]. In the case of the transmission zone plate of unity absorption in the opaque zones, one can represent the transmission function in a Fourier series expansion in terms of r^2, as suggested by Eq. (9.19).

The sketch in Figure 9.7 is useful for visualizing the Fourier decomposition and identifying the periodicity in r^2. Following Goodman,[21] we expand the transmission function in terms of γr^2, taking only odd (cosine) terms for the chosen coordinates, so that

$$f(\gamma r^2) = \sum_{m=-\infty}^{\infty} c_m \cos(m\gamma r^2) \tag{9.21}$$

where from Figure 9.7 we see[†] that $\gamma = \pi/\lambda f$. This can be written as

$$f(u) = \sum_{m=-\infty}^{\infty} c_m \cos(mu)$$

where $u = \gamma r^2 = \pi r^2/\lambda f$, and where the Fourier coefficients are given by

$$c_m = \frac{1}{2\pi} \int_{-\pi}^{\pi} f(u) \cos(mu)\, du \tag{9.22}$$

For the alternately opaque and transmissive zones of interest here the transmission function $f(u) = 1$ for $0 \le u \le \pi/2$, and $f(u) = 0$ for $\pi/2 < u \le \pi$ (see Figure 9.7), so that

$$c_m = \frac{1}{\pi} \int_0^{\pi/2} \cos mu\, du$$

[†]A radial phase shift of 2π corresponds to a difference $\Delta n = 2$ in the zone plate (one opaque, one transmissive). From Eq. (9.19), for $m = 1$, this gives an argument in the expansion parameter $\gamma(r_n^2 - r_{n-2}) = 2\lambda f\gamma = 2\pi$, or $\gamma = \pi/\lambda f$. Check this in Figure 9.7, where the phase shift between $n = 2$ and $n = 4$ corresponds to $7\pi/2 - 3\pi/2 = 2\pi$.

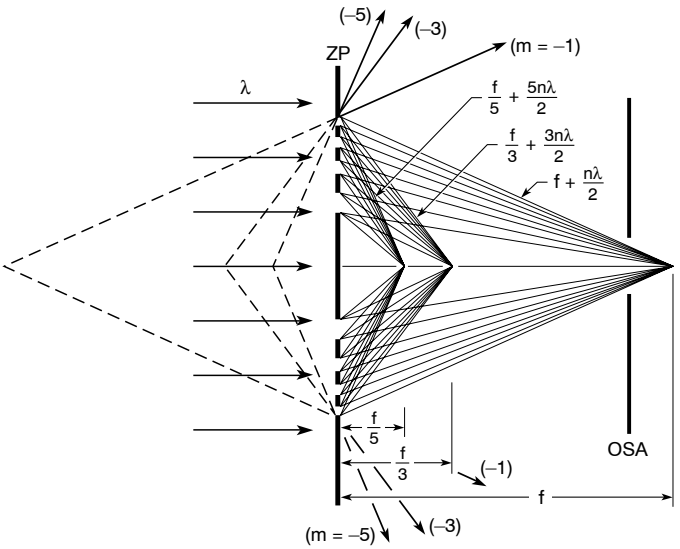

FIGURE 9.8. Zone plate diffractive focusing is illustrated for the first three positive orders. An order sorting aperture (OSA), of the type that would be used to block all but the first order, is also shown. Negative orders ($m = -1,\ -3,\ -5$) are shown as solid lines diverging from the optical axis, and projected backward to virtual foci (behind the lens) by dashed lines.

or

$$c_m = \frac{\sin(m\pi/2)}{m\pi} \tag{9.23}$$

where $m = 0,\ \pm 1,\ \pm 2,\ \pm 3, \ldots$. This is identical to the result obtained earlier for the linear transmission grating. As we observed in that case, the diffraction efficiencies to the various orders are given by [Eq. (9.16)]

$$I_m = |c_m|^2 I_0$$

so that for a Fresnel zone plate of alternately opaque and transmissive zones the diffraction efficiencies are given by

$$\eta_m = \begin{cases} \frac{1}{4} & m = 0 \\ 1/m^2\pi^2 & m \text{ odd} \\ 0 & m \text{ even} \end{cases} \tag{9.24}$$

where half the incident energy is absorbed by the opaque zones. The efficiency to the first order focus is thus about 10%, another 10% goes to the divergent $m = -1$ order, approximately 1% goes to the divergent third order ($m = 3$, virtual focus), etc., while 50% of the incident radiation is absorbed and 25% is transmitted in the forward direction ($m = 0$). As in the case of the transmission grating considered in Section 9.1, the even orders do not contribute in the symmetric case where successive zone areas are equal. The various orders are illustrated in Figure 9.8.

The decreasing efficiency with increasing order m has an interesting explanation. Within a given transmissive zone n, the even orders of m cancel at the focus, so that only odd

Chapter 10

EXTREME ULTRAVIOLET AND X-RAY LITHOGRAPHY

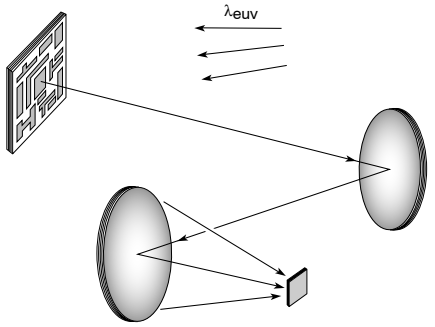

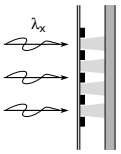

$$L_{\mathrm{w}} = k_1 \frac{\lambda}{\mathrm{NA}} \tag{10.1}$$

$$\mathrm{DOF} = \pm k_2 \frac{\lambda}{(\mathrm{NA})^2} \tag{10.2}$$

$$\sigma = \frac{\mathrm{NA}_{\mathrm{cond}}}{\mathrm{NA}_{\mathrm{obj}}} \tag{10.3}$$

$$L_{\mathrm{w}} = \alpha\sqrt{g\lambda} \tag{10.4}$$

Historically, lithography is the printing process in which an image is transferred from a flat surface, initially a smooth stone and later a metal plate, through the selective use of ink-receptive and ink-repellent treatments. Today a major application of lithography is the repetitive copying of highly detailed sub-micron spatial patterns, which after processing will form single layers of an interconnected multilevel semiconductor electronic structure commonly known as a microchip.[1] These chips are the basic building blocks of modern electronic instruments, computers, and telecommunications equipment. In this chapter we describe current state of the art lithographic equipment: deep ultraviolet (DUV) steppers that use mercury arc lamps and excimer lasers, with largely refractive optics, to print patterns with sub-quarter-micron features. The SIA Technology Road Map for Semiconductors,[2] which provides a 15-year, six-generation projection of integrated circuit (IC) characteristics, is described, with selected technical parameters for microprocessors and dynamic random access memory (DRAM) chips through the year 2012. This is followed by sections describing two candidate technologies, each of which has the potential to provide the engineering and economic solution to these